A plateau structure in the tunnelling spectrum as a manifestation of a new tunnelling mechanism in multi-dimensional barrier systems

2008 J. Phys. A: Math. Theor. 41 095101

(http://iopscience.iop.org/1751-8121/41/9/095101)

IOP PUBLISHING JOURNAL OF PHYSICS A: MATHEMATICAL AND THEORETICAL

J. Phys. A: Math. Theor. **41** (2008) 095101 (35pp) doi:10.1088/1751-8113/41/9/095101

A plateau structure in the tunnelling spectrum as a manifestation of a new tunnelling mechanism in multi-dimensional barrier systems

Kin'ya Takahashi[1] **and Kensuke S Ikeda**[2]

[1] The Physics Laboratories, Kyushu Institute of Technology, Kawazu 680-4, Iizuka 820-8502, Japan
[2] Department of Physics, Faculty of Science and Engineering, Ritsumeikan University, Noji-higashi 1-1-1, Kusatsu 525-8577, Japan

E-mail: takahasi@mse.kyutech.ac.jp and ahoo@ike-dyn.ritsumei.ac.jp

Received 23 July 2007, in final form 17 December 2007
Published 19 February 2008
Online at stacks.iop.org/JPhysA/41/095101

Abstract

In recent years a new description has been developed for tunnelling in multi-dimensional systems based on complexified stable–unstable manifolds of periodic saddles. The complexified stable–unstable manifolds guide complex-classical tunnelling trajectories over the energetic barrier (Takahashi and Ikeda 2003 *J. Phys. A: Math. Gen.* **36** 7953). In this paper it is claimed, based on theoretical analysis and numerical evidence, that the tunnelling mechanism due to complexified stable–unstable manifolds is associated with a characteristic plateau feature in the tunnelling spectrum. An analysis of a particular two-dimensional barrier tunnelling model shows that the plateau feature is obtained by a fully quantum-mechanical computation, and that the complex-semiclassical theory successfully reproduces this feature. Moreover, an analytical theory based upon Melnikov's method is developed and used to clarify quantitatively how the tunnelling mechanism due to the complexified stable–unstable manifolds leads to the formation of the plateau structure; in particular, it is shown that the classical action along the complexified stable manifold controls the height of the plateau. The analysis presented here is based on a particular model, but the main claims should hold for any system with multi-dimensional barrier tunnelling because of the universality of the underlying mechanism.

PACS numbers: 05.45.Mt, 03.65.Xp, 03.65.Sq, 05.45.−a

(Some figures in this article are in colour only in the electronic version)

1. Introduction

The understanding of tunnelling in multi-dimensional systems still remains a challenging problem. An essential difference between multi-dimensional systems and one-dimensional systems is that in general they are not integrable and they have complicated dynamical structures resulting in chaos.

In the past two decades, many theoretical and experimental studies have demonstrated remarkable effects of chaos-related dynamical structures on tunnelling processes [1–7], and theoretical investigations into typical processes such as chaos-assisted tunnelling and resonance-assisted tunnelling have been carried out [1, 2]. However, because of the difficulty of the problem, the theoretical descriptions still remain mostly at a phenomenological level based on a hybrid combination of classical, semiclassical and fully quantum approaches.

In order to achieve a complete description for non-integrable multi-dimensional tunnelling, we have to apply the complex-domain semiclassical theory [8, 9]. This has indeed been done by several authors, with some success [10–19]. However, the key mechanism driving tunnelling transport in non-integrable multi-dimensional systems has still remained unclear. This is mainly because little is known about classical chaotic dynamics which are continued analytically into the complex phase space for studying tunnelling process. What we have to do first is to find the key objects in the complexified phase space which control multi-dimensional tunnelling and to establish a clear theoretical description of them based upon investigations of minimal models.

In a previous work [19], using a periodically perturbed Eckart-type barrier system as a model system, we demonstrated that the complexified classical unstable manifold manifests itself in the tunnelling spectrum as a characteristic plateau-shaped structure. We also indicated that the underlying mechanism responsible for the formation of a plateau can be well understood by the theory of complexified stable and unstable manifolds, which our group have recently proposed as the key to understanding the mechanism of multi-dimensional tunnelling in classically nonintegrable systems [14–16, 18–20]. In this new tunnelling mechanism, the major tunnelling probability propagates along the trajectories which go through the complex phase space being guided by the complexified stable and unstable manifolds. This mechanism is quite different from the instanton mechanism in which trajectories on the complexified torus are used and which works in integrable (or very nearly integrable) systems [10]. Therefore, tunnelling phenomena caused by this new mechanism are qualitatively and quantitatively different from tunnelling phenomena caused by the instanton mechanism [21].

In the previous work [19], due to the limit length of the letter, we had to resign ourselves to showing just an outline of our theory and many important details necessary to understand how the new tunnelling mechanism works in the construction of the plateau spectrum were omitted. In this paper, we present detailed mathematical descriptions of the major theoretical arguments, which allow us to see how the complexified phase-space formalism based on the stable and unstable manifold theory works in practice.

This paper is organized as follows. In section 2, we start by introducing a 2D barrier tunnelling model, which can be considered as a minimal model of more realistic models of chemical reactions. The model consists of a single potential hump localized at the origin in the reaction coordinates Q and the channel degree of freedom (with coordinate q) described by a harmonic oscillator [22, 23]. With this model we describe the outline of the new tunnelling mechanism, explaining how the classical barrier penetration is controlled by the stable and unstable manifolds $W_{s,u}$ of the periodic orbit O, which divides product side and reactant side. Having the classical picture in mind, we next consider the tunnelling spectrum which is obtained by a fully quantum computation. It is demonstrated that, as the coupling strength

increases, the shape of the tunnelling spectrum exhibits a characteristic change from a localized narrow-band spectrum, which is explainable by the well-known instanton picture, to a novel broad-band spectrum with a remarkable plateau. Here, instead of the original 2D autonomous model, we introduce a non-autonomous model where the perturbation by the channel degree of freedom is replaced by a periodically oscillating perturbation. This non-autonomous system is the same as the one we used in the previous work [19] and well reproduces the characteristic change of the spectrum. Since the semiclassical analysis for this model is much easier than that for the original autonomous model, we use it for the theoretical analysis developed in the following sections.

In section 3, we first introduce the semiclassical S-matrix of periodically perturbed systems, which is essentially the same as Miller's classical S-matrix for multi-dimensional autonomous systems [8]. The treatment of boundary values for complexified classical trajectories contributing to the S-matrix is discussed by introducing pairwise representations for the initial values (the set $\mathcal{M}_S$) and the final values (the set $\mathcal{L}_S$) [14, 17]. Particular attention must be paid to the complex-time integration paths in the complex trajectory analysis. Choice of integration paths for the classical trajectories in relation to singularities is briefly discussed, taking the solution of the unperturbed system as a simple example. With the above preparation, the semiclassical calculation is carried out numerically. The semiclassically computed tunnelling spectrum reproduces the plateau structure of the fully quantum result very well. We demonstrate that the initial values of the tunnelling trajectories contributing to the plateau component of the spectrum form a particular subset localized in the close vicinity of the intersection between W_s and the initial manifold $\mathcal{I}$, which is defined by the input boundary condition. Focusing our attention on these characteristic subsets, we give explicit numerical evidence that the trajectories responsible for the plateau spectrum are those guided by W_s and landing close to the real space along W_u.

Section 4 is the main part of this paper, in which we develop an analytical theory explaining the numerically observed semiclassical results. First we introduce an adiabatic solution combined with the Melnikov-type analysis [18] and discuss the nature of the compexified trajectories going close to the dividing periodic orbit. Focusing our attention on the critical point, which is the above-mentioned intersection between W_s and $\mathcal{I}$, a claim is presented for a general feature of the trajectories starting in a neighbourhood close to the critical point. The claim predicts that characteristic subsets of $\mathcal{M}_S$ exist close to the critical point. Next, considering explicitly the input and output boundary conditions of the semiclassical S-matrix, we construct analytical expressions for the characteristic subsets contributing dominantly to the plateau structure. Finally, we evaluate the imaginary part of the action and the amplitude factor of the trajectories leaving from the characteristic subset and construct the S-matrix analytically. It turns out that the analytical results reproduce the whole tunnelling spectrum including the plateau structure. With all these results, though some restrictions are imposed on the coupling strength and the perturbation frequency, we achieve an analytical description for the new tunnelling mechanism induced by W_s and W_u of the dividing periodic orbit, which was first confirmed by a numerical semiclassical study.

Section 5 is devoted to summary and discussion. In particular we reinterpret our theoretical results in the 1.5D model in terms of the original 2D-autonomous model.

2. Model systems and quantum results

2.1. 2D model

We start with a model system of 2D barrier tunnelling, which is given by the following Hamiltonian [22, 23],

$$\hat{H}_{\rm tot}(Q, \hat{P}, q, \hat{p}) = \tfrac{1}{2}\hat{P}^2 + V_0(Q) + \beta v_2(Q, q) + H_{\rm ch}(q, \hat{p}). \tag{1}$$

This model can be considered to be a simplified model of a chemical reaction, e.g. collinear collision between an atom and a diatomic molecule [8, 9].

The unperturbed barrier potential $V_0(Q)$ along the reaction coordinate Q and the interaction potential $v_2(Q, q)$ between the reaction and channel degrees of freedom are chosen to be Eckart-type potentials,

$$V_0(Q) = \mathrm{sech}^2(Q), \qquad v_2(Q, q) = q\,\mathrm{sech}^2 Q. \tag{2}$$

The Hamiltonian for the channel degree of freedom is represented by the Hamiltonian for a harmonic oscillator

$$H_{\rm ch}(q, p) = \hat{p}^2/2 + \omega^2 q^2/2. \tag{3}$$

First, we consider the classical dynamics closely related to the new tunnelling mechanism. When the total energy $H(P, p, Q, q) = E_{\rm tot}$ is larger than the potential energy at its saddle point $(Q, q) = (0, 0)$, there exists an *unstable periodic cycle (saddle) O* above the top of the barrier at $Q = (0, -\beta/\omega^2)$, which is the harmonic vibration described by the Hamiltonian $H_{\rm ch}(q, p) + \beta q$ with the energy $E_{\rm tot} - 1$. It forms the transition state separating the product side from the reactant side [28, 29]. The saddle O is accompanied by the two characteristic sets called the stable manifold W_s and the unstable manifold W_u. In the classical dynamical theory of chemical reaction, W_s plays the key role. In figure 1 W_s (blue) and W_u (red) are shown in a Poincaré surface of the section Σ on the surface $q = 0$ when the total energy shell is fixed to $H(P, p, Q, q) = E_{\rm tot}$. The Poincaré surface of section is taken on the surface $q = 0$ when the trajectory crosses it with $\dot{q} > 0$.

Let us consider trajectories starting on the reactant side ($Q \to +\infty$) with constant momentum $P = P_1 (< 0)$. Then the set of initial conditions of the trajectories, denoted by $\mathcal{I}$, is the hypersurface $P = P_1$ with Q (mod$(2\pi|P_1|/\omega)$) much larger than the potential width. In figure 1 the cross-section of the set of trajectories originating from $\mathcal{I}$ is also depicted for two representative cases, namely $\mathcal{I}_a$(green) and $\mathcal{I}_b$ (purple), with the initial momentum $|P_1|$ relatively large and small, respectively. The trajectories from $\mathcal{I}_a$ intersect with W_s. The subset indicated by the green bold line passes over the barrier, corresponding to the generation of reaction products. However, when $|P_1|$ is small enough, as in the case of $\mathcal{I}_b, \mathcal{I}$ no longer intersects with W_s and there is no transport to the product side. In this regime, the reaction can only take place through tunnelling processes.

According to the conventional understanding [21], tunnelling occurs from the turning point of the real manifold (thin purple line) near O to the product side through the instanton path. However, our new tunnelling theory provides a different picture of tunnelling [14–16, 18–20]: even though W_s and $\mathcal{I}$ do not intersect in the real phase space, W_s always intersects with $\mathcal{I}$ at isolated points in the complex phase space if W_s and $\mathcal{I}$ are continued analytically into the complex domain, and there always exist complex trajectories starting close to each isolated intersection point, which go over the potential barrier towards the product side. Those trajectories are first guided by W_s, pass close to O, are repelled by it, and eventually go to infinity along W_u. In our recent studies [18, 19], we demonstrated for a periodically perturbed barrier system that such trajectories contribute dominantly to the tunnelling when the coupling strength between the reaction coordinate and the external field (interpreted as the channel coordinate for the 2D system) is strong enough.

Here in this paper we show numerical results of fully quantum calculation for $|P_1|$ less than the critical value $P_{\rm min}$ at which W_s is tangent to $\mathcal{I}$ and see how the tunnelling spectrum changes in shape with the magnitude of coupling strength, reflecting the change of the underlying classical mechanism.

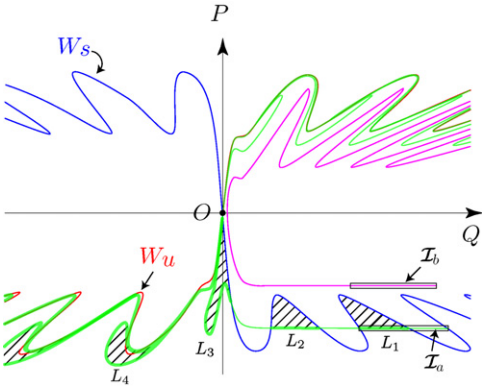

Figure 1. Classical dynamical mechanism of reaction shown on the Poincaré surface of section Σ: if W_s (blue) intersects with $\mathcal{I}_a$ (green), the shaded lobe is transported as $L_1 \to L_2 \to L_3 \ldots$. to the product side. When there is no intersection (purple), no trajectories from $\mathcal{I}_b$ can reach the product side.

First, we specify the initial state on the reactant side. Let us introduce the classical action and angle coordinates for the channel degree of freedom, namely $I = H_{\rm ch}/\omega$ and $\theta = \arctan(\omega q/p)$. Using the action and angle, (I, θ), the classical Hamiltonian is

$$H_{\rm tot}(Q, P, q, p) = \tfrac{1}{2}P^2 + V_0(Q) + \beta v_2'(Q, I, \theta) + \omega I, \tag{4}$$

where the interaction term is transformed as

$$v_2'(Q, I, \theta) = \sqrt{\frac{2I}{\omega}}\sin\theta\,\mathrm{sech}^2 Q. \tag{5}$$

For quantum calculation, we suppose that an incident wave excited as a channel eigenstate w_{n_1} with the quantum number $n_1(\geqslant 0)$ is propagating along the reaction coordinate Q from $+\infty$ with a constant momentum P_1:

$$\Psi_{\rm in} \propto \exp\{{\rm i}P_1 Q/\hbar\}w_{n_1}, \qquad Q \to +\infty. \tag{6}$$

The corresponding classical action is $I_1 = \hbar(n_1 + 1/2)$ and the total energy is given by $E_{\rm tot} = P_1^2/2 + \hbar\omega(n_1 + 1/2)$. As shown in figure 1, classical transition past the barrier is forbidden under the condition

$$E_{\rm tot} - \hbar\omega(n_1 + 1/2) < P_{\rm min}^2/2. \tag{7}$$

In this case, penetration through the product side occurs only by the tunnelling process.

Figure 2 shows typical examples of tunnelling spectra, when condition (7) holds. The fully quantum tunnelling calculation, which requires very high accuracy, was executed using the method developed in [24]. The coupling strength, which is defined as the effective perturbation strength

$$\epsilon \equiv \beta\sqrt{2I_1/\omega} = \beta\sqrt{(2n_1 + 1)\hbar/\omega}, \tag{8}$$

is varied as $\epsilon = 0.1, 0.2, 0.4$. Every spectrum is represented as a function of the kinetic energy $E_2 = P_2^2/2$ along the reaction coordinate observed in the asymptotic region on the product side. Each spectrum consists of δ-function spikes of the energy interval $\hbar\omega$, and the envelope of the spectrum changes significantly as ϵ increases: (a) in the weak perturbation regime, represented by $\epsilon = 0.1$, the envelope of the tunnelling spectrum is localized in a narrow band around the input kinetic energy $E_1\big(=P_1^2/2\big)$. (b) With a slight increase of ϵ to 0.2 a shoulder

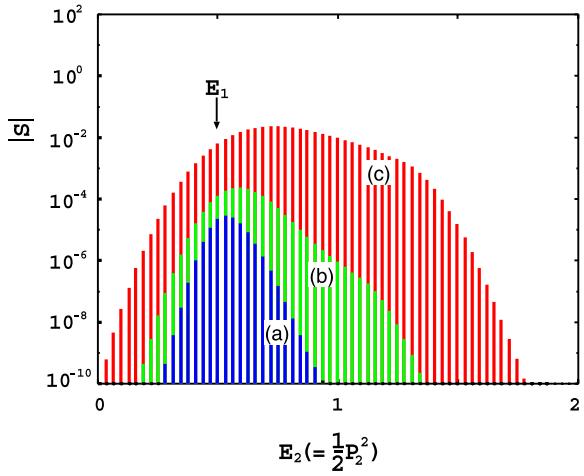

Figure 2. tunnelling spectra (absolute value of the S-matrix) of the 2D model for the three representative values of the effective perturbation strength: (a) blue $\epsilon = 0.1$, (b) green $\epsilon = 0.2$, and (c) red $\epsilon = 0.4$. $E_1 = 0.5$, $\omega = 0.3$, $n_1 = 128$ and $\hbar = 1000/(3\pi \times 2^{10}) \sim 0.1036$.

grows on the upper energy side of the main lobe. (c) At the stronger perturbation strength of $\epsilon = 0.4$, the shoulder has grown to a level similar to the main lobe and the envelope of the tunnelling spectrum spreads over a wide range of energy, forming a well-recognizable plateau. The centre of the plateau shifts to an energy value larger than the input energy E_1.

In the weak interaction regime, the fact that the reaction energy is almost conserved implies that the interaction between the two degrees of freedom at the potential hump is negligibly small and essentially one-dimensional tunnelling transmission takes place, which can be described by the instanton. However, in the strong interaction regime, the formation of a broad plateau means that an exchange of energy between the two degrees of freedom is activated when the trajectory goes through the potential barrier. The formation of a broad plateau strongly implies that a new tunnelling mechanism leading to strong mixing between the two degrees of freedom works in place of the traditional instanton mechanism.

2.2. 1.5D model

Under the assumption that the coupling strength is not very strong, so that the variation of I in the scattering process is much less than its initial value $I_1 = (n_1 + 1/2)\hbar$, the classical action can be replaced by its initial value I_1. Thus the action variable I in the interaction potential (5) can be replaced by the constant c-number I_1 and the Hamiltonian of the 2D model (4) is very well approximated as

$$H_{\rm tot}(Q, P, \theta, I) \sim \tfrac{1}{2}P^2 + V_0(Q) + \epsilon \sin\theta \,\mathrm{sech}^2(Q) + \omega I \tag{9}$$

using the perturbation strength introduced in (8). Under this approximation it is easy to see that

$$\theta = \omega t + \theta_0 \tag{10}$$

and the above Hamiltonian is equivalent to that of the periodically perturbed 1D barrier system, which we studied in the recent works [18, 19]:

$$H(Q, P, \omega t) = \tfrac{1}{2}P^2 + V_0(Q) + \epsilon v_1(Q, \omega t), \tag{11}$$

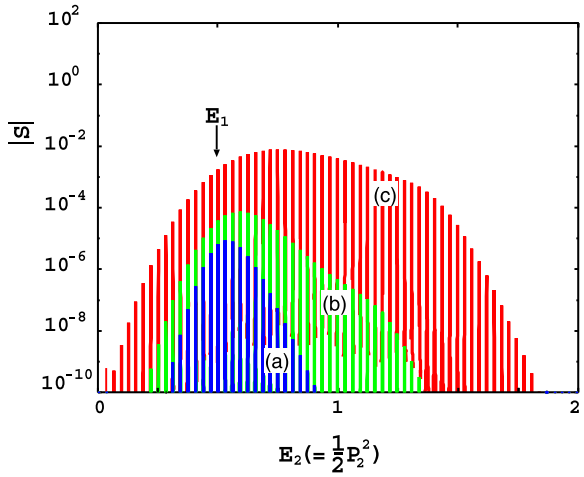

Figure 3. tunnelling spectra (absolute value of the S-matrix) of the 1.5D model for three values of ϵ: (a) blue $\epsilon = 0.1$, (b) green $\epsilon = 0.2$ and (c) red $\epsilon = 0.4$. Other parameters except for n_1 are the same as those in figure 2.

where V_0 is the same as that in the 2D model and v_1 corresponding to v_2' is replaced by the time-dependent potential

$$v_1(Q, \omega t) = \sin(\omega t)\,\mathrm{sech}^2(Q). \tag{12}$$

Here the initial phase θ_0 is set to 0 without loss of generality.

The incident wave is coming from $Q = +\infty$ with a constant momentum P_1. If the incident energy $E_1\left(=P_1^2/2\right)$ is taken such that $|P_1| < P_{\min}$, then the quantum probability observed on the transmission side is due to the tunnelling effect.

Figure 3 shows the energy spectrum of the non-autonomous 1.5D model at each of the same values of ϵ as in figure 2 [19]. In each case, the energy spectrum of the non-autonomous 1.5D model is very similar to that of the corresponding 2D model. This shows that the 1.5D model well approximates the 2D model, and the same mechanism works to cause the plateau spectrum in both the 2D and 1.5D models. Since the semiclassical analysis is much more tractable for the 1.5D model than for the full 2D model, hereafter we adopt the 1.5D model as the standard model in the following analyses.

3. Semiclassical analysis: numerical studies

3.1. S-matrix of periodically perturbed 1D systems

We start with the semiclassical expression of the S-matrix for periodically perturbed 1D systems introduced in [17], which is nothing more than the time-dependent analogue of the 'classical S-matrix' introduced by Miller for multi-dimensional autonomous systems [8]:

$$S(E_2, E_1) \sim \lim_{|Q_1||Q_2|\to\infty} \sum_{\text{c.t.}} \frac{1}{\sqrt{2\pi \mathrm{i}\hbar}} \frac{\sqrt{|P_2||P_1|}}{\sqrt{P_1 P_2}} \sqrt{-\frac{\partial^2 S_S}{\partial E_1 \partial E_2}} \times \mathrm{e}^{-\mathrm{i}(P_2 Q_2 - P_1 Q_1)/\hbar} \exp\left\{\frac{\mathrm{i}}{\hbar} S_S(Q_2, E_2, Q_1, E_1)\right\}, \tag{13}$$

where subscripts 1 and 2 of dynamical variables stand for input and output, respectively and the classical action integral is defined by

$$S_S(Q_2, E_2, Q_1, E_1) \equiv \int_{Q_1}^{Q_2} P\,\mathrm{d}Q - \int_{t_1}^{t_2} H(Q, P, \omega t)\,\mathrm{d}t + E_2 t_2 - E_1 t_1. \tag{14}$$

This is the generating function and so has the property

$$t_1 = -\frac{\partial S_S}{\partial E_1}, \qquad t_2 = \frac{\partial S_S}{\partial E_2}, \tag{15}$$

and the amplitude factor can be rewritten as

$$\sqrt{\frac{\partial^2 S_S}{\partial E_1 \partial E_2}} = \left\{ -\frac{\partial E_2(Q_2, Q_1, E_1, t_1)}{\partial t_1} \right\}^{-1/2}. \tag{16}$$

The summation $\sum_{\mathrm{c.t.}}$ should be taken over all the contributing trajectories satisfying the initial and final boundary conditions, i.e.,

$$E = E_1\big(=P_1^2/2\big), \qquad Q = Q_1(\gg 1), \tag{17}$$

$$E = E_2\big(=P_2^2/2\big), \qquad Q = Q_2(\to \pm\infty), \tag{18}$$

where $E_{1,2}$ and $Q_{1,2}$ are observables in the scattering problem and should take real values. The trajectories are calculated by the Newtonian equation of motion (or Hamilton's canonical equations).

In the tunnelling problem there are no real classical trajectories satisfying the boundary condition, but the solution is naturally extended to the complex domain, and there exist complex trajectories connecting the two boundaries and possibly contributing to the tunnelling. Once the initial boundary (17) is fixed, the trajectory can be labelled by the initial time t_1, which can be looked upon as a search parameter; namely, by moving it over the complex t_1-plane we can look for the trajectories satisfying the initial and final boundary conditions (18), although we note that this is not an easy task.

In particular, as is discussed later, the non-uniqueness of time integration paths due to the presence of singularities introduces complications coming from the multiplicity of trajectories, which is a fundamental feature of the barrier tunnelling problem.

In actual calculation, as discussed in [17], the periodicity of the perturbation helps to reduce the calculation task. Indeed, only the initial set restricted to a unit period is necessary to carry out semiclassical calculation. Thus, equation (13) can be reduced to

$$S(E_2, E_1) \sim \lim_{|Q_1||Q_2|\to\infty} \sum_n \hbar\omega\delta(E_2 - E_1 - n\hbar\omega) \sum_{\mathrm{c.t.}\in F^*} \frac{1}{\sqrt{2\pi \mathrm{i}\hbar}} \frac{\sqrt{|P_2||P_1|}}{\sqrt{P_1 P_2}} \sqrt{-\frac{\partial^2 S_S}{\partial E_1 \partial E_2}}$$
$$\times \mathrm{e}^{-\mathrm{i}(P_2 Q_2 - P_1 Q_1)/\hbar} \exp\left\{ \frac{\mathrm{i}}{\hbar} S_S(Q_2, E_2, Q_1, E_1) \right\}, \tag{19}$$

where $F^* = \{t_1 | -T \leqslant \mathrm{Re}\{t_1\} \leqslant 0, (T = 2\pi/\omega)\}$ denotes the reduced zone with the unit interval of period T. In practice, the spectrum envelope can be calculated from information for one period of the initial time t_1. The comb-like structure implied by the periodic delta functions in equation (19), which was observed also in the fully quantum spectrum, is the natural consequence of quantization of the vibronic degrees of freedom.

In the time-dependent scattering problem formulated above, the initial manifold $\mathcal{I}$ describing the set of initial conditions of classical trajectories is specified by the initial time

t_1 in addition to the fixed initial conditions $Q = Q_1(\gg 1)$ and $P = P_1$. Since t_1 is a variable search parameter in the complex domain, the initial manifold $\mathcal{I}$ can be defined by

$$\mathcal{I} = \{(t_1, Q, P) | t_1 \in \mathbf{C}, Q = Q_1(\in \mathbf{R}), P = P_1(\in \mathbf{R})\}. \tag{20}$$

To obtain the spectrum envelope one has to scan the real parameter E_2 with Q_2 fixed at a certain real number, then the search parameter t_1 will trace a 1D set on the complex t_1 plane, which has been called the $\mathcal{M}$-set [14, 17]:

$$\mathcal{M}_{\mathcal{S}} = \{t_1 \in \mathbf{C} | \mathrm{Im}\{P(t_2 - t_1, t_1, P_1, Q_1)\} = 0, Q(t_2 - t_1, t_1, P_1) = Q_2(\ll -1)\}, \tag{21}$$

where $(Q(t - t_1, t_1, P_1, Q_1), P(t - t_1, t_1, P_1, Q_1))$ is the classical trajectory leaving from (Q_1, P_1) at $t = t_1$. The $\mathcal{M}_{\mathcal{S}}$-set enables us to visualize the structure of the set of initial conditions of contributing trajectories on the search plane. The whole $\mathcal{M}_{\mathcal{S}}$-set is not a connected set but is in general composed of disjointed subsets, each of which is called a 'branch'. We also introduce the Lagrange manifold, the so-called $\mathcal{L}$-set:

$$\mathcal{L}_{\mathcal{S}} = \{(Q', P') | Q' = Q(t - t_1, t_1, P_1, Q_1), P' = P(t - t_1, t_1, P_1, Q_1), t_1 \in \mathcal{M}_{\mathcal{S}}, t \in \mathbf{R}\}. \tag{22}$$

This is a set composed of the points at which the trajectories leaving from $\mathcal{M}_{\mathcal{S}}$ arrive at a given time t. We should remark that the set $\mathcal{L}_{\mathcal{S}}$ is not, in the precise sense, the phase-space support of the semiclassical wavefunction, which was first introduced in [14]. By definition, $\mathcal{L}_{\mathcal{S}}$-set is convenient for pursuing the whole trajectories starting at the initial set.

As mentioned above, in the practical semiclassical calculation, we have to take special care of multi-valuedness of classical solutions due to the existence of singularities. The existence of singularities is generic in systems evolving with complex time and plays an important role in understanding tunnelling through barrier potentials. In the following, we briefly explain the role of singularities of the classical solution in connection with the choice of integration paths in the complex time plane by taking a static Eckart barrier as a simple example.

3.2. The static barrier and integration paths

The solution of the classical equation of motion for $0 < E_1 < 1$ at $\epsilon = 0$ is given by [8, 17]

$$Q(t - t_1, Q_1, P_1) = \sinh^{-1}(\lambda \cosh(\sqrt{2E_1}(t - t_0))), \tag{23}$$

where $\lambda \equiv \sqrt{1/E_1 - 1}$ and t_0 is the time at which the trajectory hits the turning point $Q_{\mathrm{turn}} = \pm \log[\lambda + \sqrt{\lambda^2 + 1}]$. Given initial condition $(Q = Q_1, P = P_1)$ at $t = t_1$, the asymptotic form of the solution for $t_1 - t_0 \to -\infty$ is, $Q_1 \sim \log(\lambda) - \sqrt{2E_1}(t_1 - t_0) \to +\infty$, $P_1 = -\sqrt{2E_1}$, and the relation between t_0 and t_1 is given by $t_0 - t_1 = (Q_1 - \log\lambda)/\sqrt{2E_1} \equiv t_{01}$. For convenience of analysis, let us introduce the lapse time $s = t - t_1$. In the lapse time the solution has singularities at

$$Sg_n^{\pm} = (Q_1 - \log\lambda)/\sqrt{2E_1} \pm \frac{1}{\sqrt{2E_1}} \sinh^{-1}(1/\lambda) + \mathrm{i}(-n + 1/2)\Delta t_I/2, \quad (\Delta t_I \equiv 2\pi/\sqrt{2E_1}). \tag{24}$$

As shown in figure 4, singularities aligned along two lines i.e. entrance singularities Sg_n^- and exit singularities Sg_n^+, and the representative integration paths labelled 'C_n'(n: integer) have different topology with respect to the singularities. Trajectories defined along the integration paths homotopic to C_{2n+1}'s make contributions to the tunnelling component, while trajectories along C_{2n}'s are reflected by the potential barrier [18].

A trajectory defined along any integration path C_n contributes to either a reflected component or a tunnelling component, but the major contributions come from trajectories

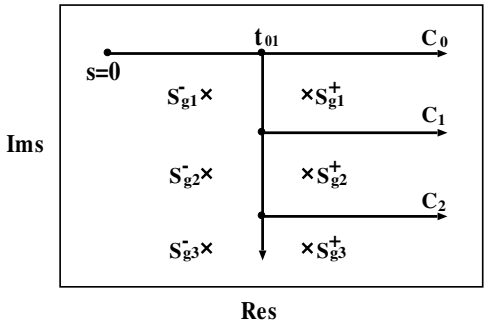

Figure 4. Singularities and representative integration paths on the lapse time plane.

along the lowest order paths closest to the real axis, namely, C_0 (reflection) and C_1 (tunnelling). Trajectories along higher order paths $C_2, C_3, \ldots$ have larger imaginary parts in their classical actions, and their contributions are exponentially smaller than the lowest order contributions in the semiclassical limit ($\hbar \to 0$) and thus may be neglected.

3.3. Semiclassical results in the strong perturbation regime

As shown in [18] and briefly mentioned in subsection 2.1, the nature of the classical solution is much disturbed in the complex domain, once the periodic perturbation is applied. The initial manifold $\mathcal{I}$ defined by equation (20) always intersects with W_s at some complex initial times $t_1 = t_{1c}$'s in the complex domain, even when the perturbation strength ϵ or the input energy E_1 is so small that there is no intersection between W_s and $\mathcal{I}$ in the real domain. In accordance with [18], we call t_{1c} *critical point*. In fact, as was shown by using a Melnikov-like perturbation method extended into the complex domain in [18], the intersections t_{1c}'s always exist and the imaginary part of t_{1c} is given by

$$\mathrm{Im}\, t_{1c} = \frac{1}{\omega}\cosh^{-1}\left\{\frac{1-E_1}{\epsilon(1-\chi(\omega))}\right\} \tag{25}$$

within the framework of perturbation theory, where χ is defined by

$$\chi(\omega) \equiv 2\omega \int_0^\infty \frac{\sin \omega s}{1+\mathrm{e}^{2\sqrt{2}s}}\,\mathrm{d}s. \tag{26}$$

Note that due to the periodicity of perturbation, the critical points t_{1c}'s appear periodically with the period of the perturbation T with the same value in imaginary part (25). Equation (25) tells that the critical point t_{1c} is deep in the imaginary plane if the perturbation strength ϵ is small enough. Then the trajectory along the lowest order integration path C_1 may not be affected by the critical point. This is the case of the weak perturbation regime, in which the perturbation expansion approach taking the instanton trajectory as the zeroth-order solution works very well [25].

However, as ϵ increases the critical point moves towards the real axis and its imaginary part becomes comparable in magnitude with the lowest order path C_1, which drastically disturbs the original nature of tunnelling trajectories along C_1. This is the typical situation in the 'strong perturbation regime', where the plateau spectrum emerges [18].

Now, let us show numerical results for the semiclassical S-matrix. Figure 5 indicates a typical example of the $\mathcal{M}_S$-set obtained in the strong perturbation regime. On the t_1-plane, we also find the critical point t_{1c} indicated by an X. As discussed in section 3.1, the $\mathcal{M}_S$-set

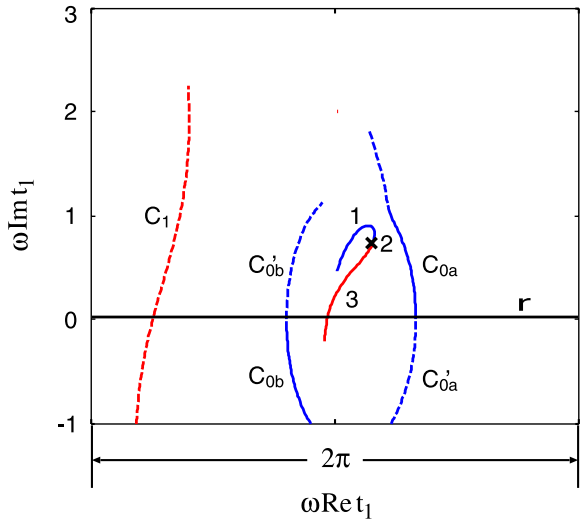

Figure 5. $\mathcal{M}_S$-set for the S-matrix. Red curves are the complex branches contributing to tunnelling, while the blue branches contribute to reflection and the black line labelled 'r' is the real branch making reflection. Parts of branches drawn by broken lines indicate non-contributing parts which are removed by the proper treatment of the Stokes phenomenon [15, 17, 26].

in the reduced zone is enough to calculate the spectrum's envelope, and so we show only one cycle.

There are a number of branches on the t_1-plane, whose structure seems to be rather complicated. Among them, only a few branches close to the critical point, namely branches 1, 2 and 3, make major contributions to the tunnelling. Those branches exhibit interesting structure in the neighbourhood of the critical point.

Figure 6(a) is a magnification of the area close to the critical point t_{1c}. The branches consist of a straight line passing through t_{1c} and a circle centred at t_{1c}. We denote the straight line branch and the circle branch by $\mathcal{M}_\mathcal{R}$ and $\mathcal{M}_\mathcal{C}$, respectively. Two cuts indicated by wavy lines transverse $\mathcal{M}_\mathcal{C}$, and they divide $\mathcal{M}_\mathcal{C}$ into a pair of semicircles. Then the upper part and the lower part of $\mathcal{M}_\mathcal{C}$ should go into different Riemann sheets across the cuts, and the two parts make different contributions to the S-matrix. That is, trajectories starting from all the branches in the upper half-plane above the two cuts reach the reflective side, while trajectories in the lower half-plane go to the transmissive side.

The corresponding $\mathcal{L}_\mathcal{S}$-set projected on the real phase space in figure 6(b) helps us to see the asymptotic behaviour of those trajectories in the limit $\mathrm{Re}\, t \to \infty$. The Lagrange manifold $\mathcal{L}_\mathcal{R}$ corresponding to $\mathcal{M}_\mathcal{R}$ is extended into both the transmissive and reflective sides along the real unstable manifold indicated by W_{uR}. Thus, most of the trajectories starting from $\mathcal{M}_\mathcal{R}$ reach very close to W_{uR}. Note that the destination of the trajectory changes as the initial value t_1 moves along $\mathcal{M}_\mathcal{R}$ passing through t_{1c}. Therefore, the branch $\mathcal{M}_\mathcal{R}$ is regarded as a *merged* object composed of the tunnelling and the reflective branches of the unperturbed system. Indeed, the topology of the time integration path switches from C_1-like to C_2-like (and vice versa) as t_1 moves along $\mathcal{M}_\mathcal{R}$ passing through the critical point. This drastic phenomenon is induced by a divergent motion of the time singularities Sg_n^+'s: they are 'movable' depending upon t_1 in periodically perturbed systems and diverge at $t_1 = t_{1c}$ [18].

On the other hand, the Lagrange manifold $\mathcal{L}_\mathcal{C}$ of $\mathcal{M}_\mathcal{C}$ forms whiskers extending from apexes and anti-apexes of oscillating $\mathcal{L}_\mathcal{R}$, which extend deep into the imaginary sides along

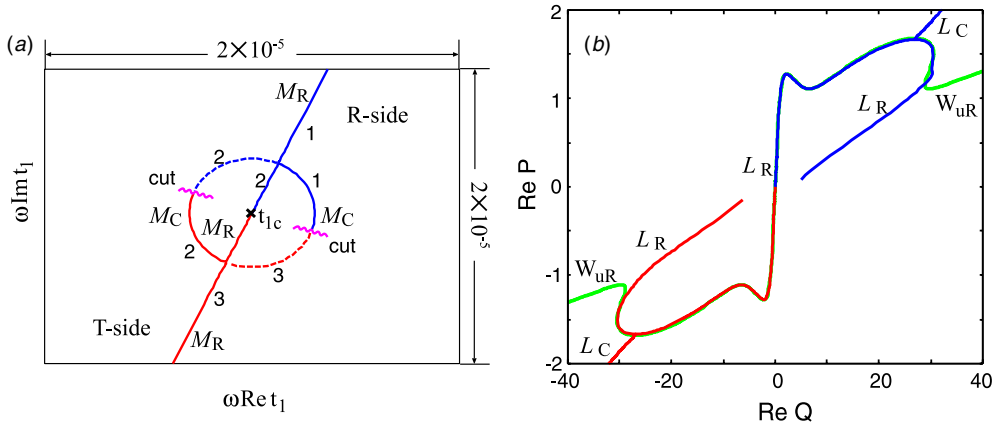

Figure 6. Characteristic branches $\mathcal{M}_{\mathcal{R}}$ and $\mathcal{M}_{\mathcal{C}}$ and corresponding $\mathcal{L}_{\mathcal{S}}$-set, $\mathcal{L}_{\mathcal{R}}$ and $\mathcal{L}_{\mathcal{C}}$. (*a*) Magnified view of $\mathcal{M}_{\mathcal{S}}$-set near the critical point. (*b*) $\mathcal{L}_{\mathcal{S}}$-set projected on the real space. W_{uR} (green thin curve) indicates the real unstable manifold.

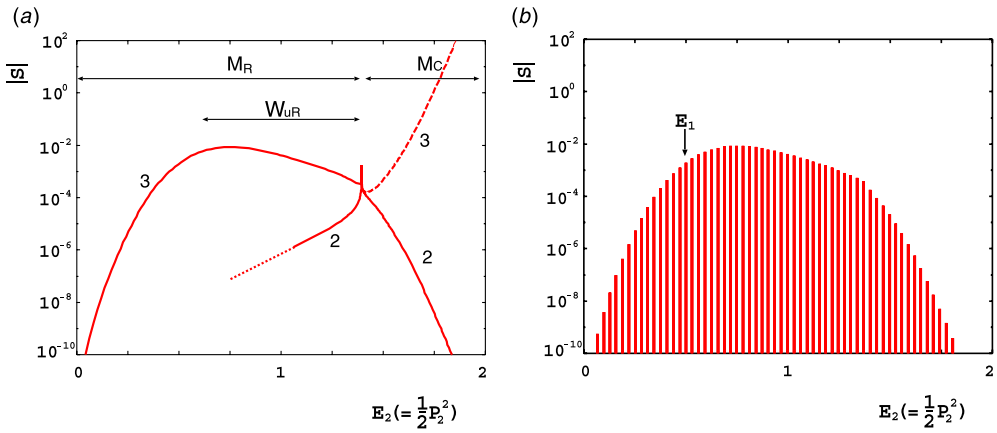

Figure 7. Semiclassical results: (*a*) weights of major contributing branches. The right–left arrow indicated by W_{uR} means the energy range covered by the real unstable manifold (see figure 6). The parts contributed by $\mathcal{M}_{\mathcal{R}}$ and $\mathcal{M}_{\mathcal{C}}$ are also indicated. A short spike at $E_2 \sim 1.4$ is an artifact due to the semiclassical error close to the caustic between branches 2 and 3. (*b*) Resultant energy spectrum.

the complex unstable manifold. Paired parts of branches in $\mathcal{M}_{\mathcal{C}}$ which are symmetric with respect to $\mathcal{M}_{\mathcal{R}}$ in the same semicircle form paired branches in the $\mathcal{L}_{\mathcal{S}}$-set, which are almost complex conjugate, so that they seem to be degenerate when projected onto the real phase space. Note that one of the paired parts taking negative values in the imaginary part of the classical action is removed by a proper treatment of the Stokes phenomenon to kill its unphysical contribution [15, 17, 26].

In order to reconstruct the plateau spectrum semiclassically, all we have to do is to take account of just the contributions from $\mathcal{M}_{\mathcal{R}}$ and $\mathcal{M}_{\mathcal{C}}$ on the transmissive side, namely the branches 2 and 3 in the original picture. Figure 7(*a*) shows semiclassical weights of the branches 2 and 3 as functions of E_2. It shows that the branches in $\mathcal{M}_{\mathcal{R}}$ form the main part of the spectrum, i.e., the flat top of the plateau whose width corresponds to the

amplitude of the oscillation in momentum of the real unstable manifold on the asymptotic side. Figure 7(*b*) shows the energy spectrum reconstructed by summing up the weights of the contributing branches. Its agreement with the pure quantum result in figure 3 is very good.

It is concluded that the tunnelling trajectories making major contribution to the plateau spectrum, which start at $\mathcal{M}_{\mathcal{R}}$ (and $\mathcal{M}_{\mathcal{C}}$) in the close neighbourhood of t_{1c}, are first guided by the complexified stable manifold and finally reach close to the real plane following the real (and complex) unstable manifold. Therefore the plateau is a manifestation of the unstable manifold in the tunnelling effect.

4. Semiclassical analysis: analytical treatment

4.1. Low-frequency approximation

The numerical calculation in section 3.3 shows that the tunnelling trajectories making major contribution to the plateau spectrum in the strong perturbation regime are due to the new tunnelling transport mechanism supported by the complexified stable–unstable manifolds. In the present section, assuming that the perturbation is sufficiently slowly varying, i.e., $\omega \ll 1$, we develop an analytical theory to answer why the characteristic branches $\mathcal{M}_{\mathcal{R}}$ and $\mathcal{M}_{\mathcal{C}}$ appear in the close neighbourhood of the critical point and how they contribute to the formation of the plateau. Our analysis is based on an analytical solution of the classical equation of motion which was introduced in [18] to clarify the mechanism of the fringed tunnelling. First, we review main features of the analytical solution.

The analytical solution is obtained as a natural extension of the unperturbed solution (23):

$$Y(t) \equiv \sinh Q = r(t)\cosh\phi(t). \tag{27}$$

The solution satisfies the classical equation of motion derived from the classical Hamiltonian (11),

$$\ddot{Q} = 2a(t)\frac{\sinh Q}{\cosh^3 Q}, \tag{28}$$

where

$$a(t) \equiv 1 + \epsilon \sin\omega t. \tag{29}$$

On the assumption that $\omega \ll 1$, the equations

$$\dot{\phi}(t) = \sqrt{2E(t)}, \tag{30}$$

$$\frac{\mathrm{d}}{\mathrm{d}t}\{r(t)^2\dot{\phi}(t)\} = 0, \qquad \text{namely} \quad r(t) = \frac{\alpha}{\{2E(t)\}^{1/4}}, \tag{31}$$

hold and the term containing the higher-order time derivative of the slowly varying amplitude ($\ddot{r}$) is ignored. In the unperturbed system, when taking the limit $\lambda \to 0$, the exact solution (23) gives the orbits approaching O in forward and backward time evolutions, namely solutions on the stable and unstable manifolds. In the solution (27), λ is replaced by $r(t)$ and the parameter α plays the same role as the λ, namely the parameter α measures the distance of the trajectory from the unstable saddle O. Since we are interested in the trajectories going close to the saddle, α^2 is taken to be a very small parameter.

This set of equations (30) and (31) is insufficient for providing a closed form solution: integrating equation (30) requires $E(t)$ to be an explicit function of t. Thus the energy $E(t)$ is determined by using the energy equation of motion

$$\dot{E} = \frac{\partial H}{\partial t} = \frac{\dot{a}(t)}{\cosh^2 Q} = \dot{a}(t)V_0(Q), \tag{32}$$

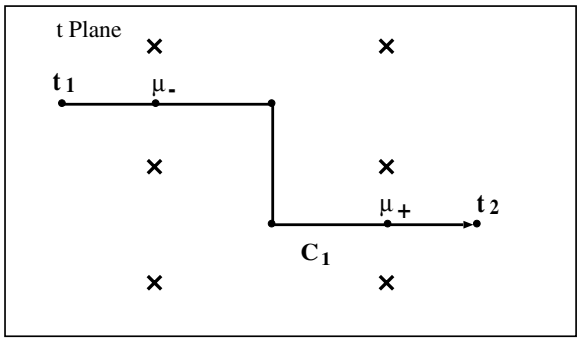

Figure 8. Positions of the gates $\mu_{\mp}$ in the complex time plane.

as a supplementary equation. We integrate the energy equation by approximating $Q(t)$ with the unperturbed solution given by equation (23), according to the spirit of Melnikov's perturbation theory. Therefore, we suppose that the parameter ϵ is small enough in the following arguments. The integration is performed along the time integration path which is topologically the same as the lowest order tunnelling path C_1 of the unperturbed system. For treating the analytical solution, it is convenient to introduce the particular times called 'gates', $\mu_{\mp}$, which respectively mean the entrance and exit of the scattering region where the perturbation has most effect. The 'gate' times are defined as the times at which the potential varies most steeply, namely

$$\mathrm{d}^2 V_0(Q(t))/\mathrm{d}t^2|_{t=\mu_{\mp}} = 0, \tag{33}$$

which leads to more explicit conditions for them:

$$\mathrm{e}^{\mp\phi(\mu_{\mp})} = 2\mathrm{e}^{\mathrm{i}n_{\mp}\pi}[1 + r(\mu_{\mp})^2/4]/r(\mu_{\mp}), \tag{34}$$

where $n_{\mp}$ are integers determined by the relative positions of $\mu_{\mp}$ to the entrance and exit singularities, respectively. Figure 8 shows the positions of $\mu_{\mp}$ on the integration path C_1 together with the singularities, marked by 'x', on the complex t-plane. The path C_1 can be deformed without changing its topology with respect to the singularities so that it passes through the gates $\mu_{\mp}$ adjacent to it.

Integrating the energy gain equation (32) by using the unperturbed solution (23) for $Q(t)$ (the Melnikov's method, see appendix A), the expressions for the energy in the input asymptotic region, inside the two gates and in the output asymptotic region are respectively given by

$$E(t) = \begin{cases} h_0 a(\mu_-) & (\mathrm{Re}\, t \ll \mathrm{Re}\, \mu_-) \\ h_0 a(t) & (\mathrm{Re}\, \mu_- < \mathrm{Re}\, t < \mathrm{Re}\, \mu_+) \\ h_0 a(\mu_+) & (\mathrm{Re}\, t \gg \mathrm{Re}\, \mu_+). \end{cases} \tag{35}$$

Here $h_0 = V_0(Q(t_0))$ is the value of unperturbed potential energy at the particular time t_0 between the two gates, which is considered as the time origin of the solution so that the phase $\phi(t)$ vanishes at $t = t_0$, i.e., $\phi(t_0) = 0$, and

$$h_0 \sim 1 - \alpha^2/\sqrt{2}. \tag{36}$$

Equation (35) tells us that the energy in each asymptotic region is determined by the energy at the corresponding gate.

Using equation (35) in equation (30), the explicit expressions for the phase $\phi(t)$ follow: in the time region bounded by the two gates, i.e., $\mathrm{Re}\, \mu_- < \mathrm{Re}\, t < \mathrm{Re}\, \mu_+$,

$$\phi(t) = \int_{t_0}^{t} \sqrt{2a(s)h_0}\, \mathrm{d}s, \tag{37}$$

and in the input and output asymptotic regions, i.e., $\mathrm{Re}\, t < \mathrm{Re}\, \mu_-$ or $\mathrm{Re}\, t > \mathrm{Re}\, \mu_+$,

$$\phi(t) = \int_{t_0}^{\mu_\mp} \sqrt{2a(s)h_0}\, \mathrm{d}s + \sqrt{2a(\mu_\mp)h_0}(t - \mu_\mp). \tag{38}$$

With these relations, one can obtain an explicit expression for the adiabatic solution.

In the asymptotic regions, by substituting equations (35) and (38) into the solution (27) and using (34) and the input boundary conditions

$$E(t_1) = a(\mu_-)h_0 = E_1, \qquad Q(t_1) = Q_1, \tag{39}$$

the explicit relation between the entrance gate and the initial time is obtained,

$$\sqrt{2E_1}(t_1 - \mu_-) + Q_1 = \log 2 + \alpha^2[4\sqrt{2E_1}] + O(\epsilon\omega), \tag{40}$$

where the dominant term in the neglected terms of $O(\epsilon\omega)$ is proportional to $\dot{a}(\mu_-)/\sqrt{E_1}$.

Equations (39) and (40) provide a set of equations determining t_1 and μ_- as functions of the smallness parameter α. Let t_{1c} and μ_{-c} be the values of t_1 and μ_- for $\alpha = 0$, then the relations

$$\alpha^2 = A_1(t_1 - t_{1c}) = A_2(\mu_- - \mu_{-c}) \tag{41}$$

hold, where A_1 and A_2 are nearly equal constants:

$$A_1 \sim A_2 \sim \sqrt{2}\frac{\mathrm{d}a(\mu_-)}{\mathrm{d}\mu_-}\bigg|_{\mu_- = \mu_{-c}} \sim O(\epsilon\omega). \tag{42}$$

Recalling that the adiabatic solution represents the stable manifold in the limit $\alpha \to 0$, t_{1c} is the time at which a trajectory on W_s hits (Q_1, P_1), and thus it is the critical point. Equation (41) gives an important relation between the initial time measured from the critical point $t_1 - t_{1c}$ and the smallness parameter α^2. We note here that μ_{-c}, which is the entrance gate along the critical trajectory launched at t_{1c}, satisfies

$$a(\mu_{-c}) = E_1. \tag{43}$$

Using equations (34) and (37) yields another important relation between the two gates

$$\mu_+ - \mu_- \sim -\tfrac{1}{\sqrt{2}} \log \alpha^2 + \tfrac{1}{\sqrt{2}}\{\log 2^{5/2} - in\pi\} + \Delta\mu(\mu_-, \mu_+), \tag{44}$$

where $\Delta\mu(\sim O(\epsilon/\omega))$ is a periodic function of both μ_- and μ_+ with the period $T(=2\pi/\omega)$, and the integer n is determined by $n = -(n_+ + n_-)$, which, as shown in the next subsection, defines the destination of the trajectory, reflective or transmissive side. The physical meaning of equation (44) is evident: it takes a logarithmically long time for a particle to pass through the scattering region as the trajectory comes close to O. Now, all the tools necessary for discussion in the following subsections have been provided.

4.2. Trajectories starting in the close neighbourhood of the critical point

In this subsection we first provide the explicit expressions for the adiabatic solution and discuss their properties. Then, we discuss the key role played by the critical point in the formation of tunnelling paths, which seems to be quite universal in the barrier tunnelling problem.

In order to clarify the roles of stable and unstable terms in the solution more explicitly, we introduce a new phase into which the amplitude factor is incorporated:

$$\varphi_-(t) = \phi(t) + \log 2 - \log\{\alpha(2E(t))^{-1/4}\}. \tag{45}$$

Then the adiabatic solution is reduced to

$$Y(t) = \sinh Q(t) = \alpha^2\, \mathrm{e}^{\varphi_-(t)}/(4\sqrt{2E(t)}) + \mathrm{e}^{-\varphi_-(t)}. \tag{46}$$

Substituting the expression of $E(t)$ given by the Melnikov method (see equation (76)) into equation (30) and integrating it while keeping lowest order terms of ϵ, ω and α^2, the explicit expression for φ_- [18] is obtained:

$$\varphi_-(t) = \begin{cases} \sqrt{2E_1}(t - t_1) - Q_1 + \log 2 + O(\epsilon\omega) & (\text{if } \operatorname{Re} t \leqslant \operatorname{Re} \mu_-) \\ \displaystyle\int_{\mu-}^{t} \sqrt{2a(s)h_0}\,\mathrm{d}s + \varphi_-(\mu_-) + O(\epsilon\omega) & (\text{if } \operatorname{Re} \mu_- \leqslant \operatorname{Re} t \leqslant \operatorname{Re} \mu_+) \\ \sqrt{2a(\mu_+)h_0}(t - \mu_+) + \varphi_-(\mu_+) + O(\epsilon\omega) & (\text{if } \operatorname{Re} t \geqslant \operatorname{Re} \mu_+). \end{cases} \tag{47}$$

At $t = \mu_-$, $\varphi_-(t)$ takes a small value except for the correction of $O(\alpha^2)$ or $O(\epsilon\omega)$:

$$\varphi(\mu_-) \sim O(\alpha^2) + O(\epsilon\omega) \tag{48}$$

which means that we move the origin of time to the entrance gate.

As equation (47) implies, $\varphi_-(t)$ oscillates in the scattering region $\operatorname{Re} \mu_- \leqslant \operatorname{Re} t \leqslant \operatorname{Re} \mu_+$, but, if ϵ is small enough, it is essentially a monotonically increasing function of $\operatorname{Re} t$ as in the case of the unperturbed limit $\epsilon = 0$. In the forward time evolution, the solution is represented as a sum of an exponentially decaying stable term and an exponentially growing unstable term to which the smallness parameter α^2 is multiplied. In the limit $\alpha^2 \to 0$, only the stable term $\mathrm{e}^{-\varphi_-(t)}$ survives, which represents a trajectory converging to $O = (0, 0)$, and so the trajectory of $\alpha = 0$ is on the stable manifold W_s of O.

If $|\alpha^2|$ is very small but finite, there exists a time regime in which the contributions of the stable and unstable terms both become very small and the trajectory comes close to the point O. In such a time regime we have a linearized solution:

$$(Q(t), P(t)) = (\alpha^2\,\mathrm{e}^{\varphi_-(t)}/4\sqrt{2a(t)} + \mathrm{e}^{-\varphi_-(t)}, \alpha^2\,\mathrm{e}^{\varphi_-(t)}/4 - \sqrt{2a(t)}\,\mathrm{e}^{-\varphi_-(t)}). \tag{49}$$

It is worthwhile remarking on the meaning of the imaginary time evolution due to the detour of the integration path C_n into the imaginary side (see figure 8). It may take place in the linear regime in which the exponential growth of the unstable term in equation (49) occurs. Then it is evident that the imaginary evolution induces a rotation in the complex-Q plane (and in the P plane as well). From equation (47) the change of φ_- in the imaginary time evolution is roughly estimated by $\mathrm{i}\sqrt{2} \times \operatorname{Im} \Delta t$, where Δt is the increment of time.

In the forward time evolution beyond the exit gate, namely $\operatorname{Re} t > \operatorname{Re} \mu_+ \sim -\operatorname{Re} \log(\alpha^2/2^{5/2})/\sqrt{2} + \mu_-$ (see equation (44)), the exponentially growing unstable term overcomes the decaying stable term. In order to explore the asymptotic behaviour in this regime, it is convenient to introduce the counterpart of φ_- at the exit, which is defined by

$$\varphi_+ \equiv \phi(t) - \log 2 + \log\{\alpha(2E(t))^{-1/4}\}. \tag{50}$$

Then the solution (27) is reduced to

$$Y(t) = \sinh Q(t) = \mathrm{e}^{\varphi_+(t)} + \alpha^2\,\mathrm{e}^{-\varphi_+(t)}/(4\sqrt{2E(t)}). \tag{51}$$

It is the exit version of equation (46) emphasizing the unstable term. Like $\varphi_-(t)$, $\varphi_+(t)$ can be also regarded as a monotonically increasing function with $\operatorname{Re} t$ and the real part of φ_+ takes a small value at $t = \mu_+$, but it has a finite imaginary part. Indeed it takes $\varphi_+(\mu_+) \sim -\mathrm{i}n\pi$ at $t = \mu_+$, where the index n is the same as the integer n in equation (44), which is confirmed by combining equations (44), (45), (47), (48) and (50). The index n plays a quite important role: the sign of that unstable term $\mathrm{e}^{\varphi_+(t)}$, which in the limit $\operatorname{Re} t \to +\infty$ dominates the behaviour of $Q(t)$, is determined by $\operatorname{Im} \varphi_+$ at $t = \mu_+$ such that $\mathrm{e}^{-\mathrm{i}n\pi} = (-1)^{-n}$, and hence the destination of the trajectory is controlled by n; the transmissive side for odd n and reflective side for even n.

The trajectory in the exit range $\mathrm{Re}\, t > \mathrm{Re}\, \mu_+$ behaves symmetrically with respect to the entrance range $\mathrm{Re}\, t < \mathrm{Re}\, \mu_-$. First, the system behaves as a free particle in the range $\mathrm{Re}\, t > \mathrm{Re}\, \mu_+$, where φ_+ is represented as

$$\varphi_+(t) \sim \sqrt{2E_\infty}(t - \mu_+) - \mathrm{i}n\pi, \tag{52}$$

where E_∞ is the energy in the asymptotic region. Thus, in the limit of $\mathrm{Re}\, t \to \infty$, equation (51) is approximated as

$$Q \sim \pm\sqrt{2E_\infty}(t - \mu_+) + \log 2. \tag{53}$$

On the other hand, from the last equation of equation (35), the energy in the exit range $\mathrm{Re}\, t > \mathrm{Re}\, \mu+$ is also determined by

$$E_\infty = a(\mu_+)(1 - \alpha^2/\sqrt{2}), \tag{54}$$

which is symmetrical to the first equation of equation (39) in the entrance range.

On the other hand, by letting $\alpha^2 \to 0$, the solution (51) represents the trajectory converging to O in the backward time evolution and hence the trajectory is on the unstable manifold W_u. Let μ_{+c} be μ_+ of the trajectory labelled by $\alpha^2 = 0$. Then it plays the same role as μ_{-c} of the trajectory on W_s and identifies the trajectory on W_u, and symmetrically to equation (43), it is related to asymptotic energy E_∞ by

$$E_\infty = a(\mu_{+c}). \tag{55}$$

Therefore, similarly to equation (41), the relation

$$\alpha^2 = A_2'(\mu_+ - \mu_{+c}) \tag{56}$$

holds, where $A_2' = \sqrt{2}\frac{\mathrm{d}a(\mu_+)}{\mathrm{d}\mu_+}\big|_{\mu_+=\mu_{+c}} \sim O(\epsilon\omega)$.

Let $U(\rho)$ be a neighbourhood close to t_{1c} with a small enough radius ρ:

$$U(\rho) = \{t_1 \in \mathbf{C} | |t_1 - t_{1c}| < \rho\}. \tag{57}$$

Then the smallness parameter characterizing the trajectory satisfies $|\alpha^2| < \rho|A_1|$.

From equations (41) and (56) we find that a trajectory starting at any initial time t_1 in $U(\rho)$ is always connected to a nearby trajectory on W_u at the exit of the scattering region with the same output energy E_∞. Since from equation (53) the system behaves as a free particle beyond μ_+(or μ_{+c}) with a fixed momentum, the distance between those two trajectories is determined by the separation of the coordinates at the exit gate

$$|\delta Q| \sim |\sqrt{2E_\infty}(\mu_+ - \mu_{+c})| \sim |\sqrt{2E_\infty}\alpha^2/A_2'|, \tag{58}$$

where use is made of equation (56), and it keeps the same level of separation even at $\mathrm{Re}\, t \to +\infty$. From equation (41), taking t_1 closer to t_{1c}, the trajectory reaches closer to W_u, but it spends a longer time in the scattering region (see equation (44)) before it arrives at the asymptotic region.

The above results are summarized as follows:

the trajectory leaving from (Q_1, P_1) *at* $t_1 \in U(\rho)$ *travels close to* W_u *in the asymptotic region in the limit* $\mathrm{Re}\, t \to \infty$.

We stress here that W_u in the above claim is the complexified unstable manifold. We can prove that a converse claim also holds, if the phase space under consideration is restricted to a certain finite imaginary domain:*close to* W_u*, there always exists a trajectory leaving from* (Q_1, P_1) *at* $t_1 \in U(\rho)$.

Although we do not have enough space to give the detailed proof of the latter claim, we can present a sketch of the proof as follows. Let $S_t(\rho)$ be the set composed of the

end points of all the trajectories at t, which start from (Q_1, P_1) at $t_1 \in U(\rho)$. Then the set $S_t(\rho)$ is transported towards O travelling along by the critical trajectory leaving from (Q_1, P_1) at $t = t_{1c}$ and travelling on W_s. At an appropriately chosen time t^*, $S_t(\rho)$ comes close to O, where the trajectory is approximated by equation (49) in the linear regime. Since $\mu_- = \mu_{-c} + O(|\alpha|^2/\epsilon\omega)$, the small stable term $\mathrm{e}^{-\varphi_-(t^*)}$ is common for all the points in $S_{t^*}(\rho)$. If we neglect the stable term in equation (49), all the points on $S_{t^*}(\rho)$ are translated to W_u to form a subset of the local unstable manifold around O. We denote this subset by $W_u^*(\rho)$, which is a disc with radius $r^* \sim \rho|A_1|/d^*(\ll 1)$ centred at O because $|\alpha^2| < \rho|A_1|$ for trajectories of $t_1 \in U(\rho)$, where $d^* \sim \mathrm{e}^{-\varphi_-^*}$ measures the distance between $S_{t^*}(\rho)$ and $W_u^*(\rho)$. As a result, by reducing ρ with fixing the radius $r^*(\ll 1)$ small enough (this means to increase $\mathrm{Re}\, t^*$), we can make $S_{t^*}(\rho)$ approximate $W_u^*(\rho)$ to any desired accuracy, namely within the precision of $d^* \sim \rho|A_1|/r^*$. This is nothing more than the well-known λ lemma extended in the complex domain. Observing further the time evolution of $S_{t^*}(\rho)$ and $W_u^*(\rho)$, it can be shown that, for any point $Z \in W_u^*(\rho)$, one can find a point $Z' \in S_{t^*}(\rho)$ such that the distance between the two forward trajectories emanating from Z and Z' is of $O(|\alpha^2|/\epsilon\omega)$, which is less than const. $\times\, \rho$. This comes from the fact that one can make the asymptotic momentum of the trajectory from Z' equal to that of the trajectory from Z. Noting that the unstable manifold W_u is obtained by the forward time evolution of $W_u^*(\rho)$ and that the distance can be made arbitrarily small by reducing ρ, then we arrive at the desired claim mentioned above.

The above claims provide a clear basis for conjecturing the nature of $\mathcal{M}_S$, namely, the set of the initial points of trajectories contributing to the semiclassical S-matrix. From the output boundary condition (18), the final manifold $\mathcal{F}$ on which the contributing trajectories should land is given by

$$\mathcal{F} = \{(t, Q, P) \mid t \in \mathbf{C}, Q = Q_2(\in \mathbf{R}), P = P_2(\in \mathbf{R})\}, \tag{59}$$

which is the counterpart of the initial manifold $\mathcal{I}$ (20) at the exit. To reproduce the tunnelling spectrum, the real-valued momentum P_2 is varied with the fixed Q_2 on the product side. If the complexified W_u intersects with $\mathcal{F}$ at $t = t_2$ for a certain value of P_2, there should exist a trajectory starting in $U(\rho)$ and landing at a neighbouring point of the intersection on $\mathcal{F}$. This is the essence of the new tunnelling mechanism, which would seem to be generic in the multi-dimensional barrier tunnelling process. Since W_u contains the real unstable manifold W_{uR} as a subset, $\mathcal{F}$ has to intersect with W_{uR} at a real-valued t_2 in a relevant range of $P_2(\in \mathbf{R})$. On the other hand, the complementary component $W_u - W_{uR}$ can also intersect with $\mathcal{F}$ for some other ranges of P_2. Corresponding to the two types of the intersection $W_u \cap \mathcal{F}$, contributing trajectories starting in $U(\rho)$ are categorized into two types according to their intersection with $\mathcal{F}$:

(1) the intersection with $\mathcal{F}$ is close to $W_{uR} \cap \mathcal{F}$, where the arrival time t_2 is complex but is expected to be very close to a real value.
(2) the intersection is close to $(W_u - W_{uR}) \cap \mathcal{F}$, and thus the arrival time t_2 can have a significantly large imaginary part.

In the next section, we show that the two types of characteristic branches $\mathcal{M}_\mathcal{R}$ and $\mathcal{M}_\mathcal{C}$, which we have encountered in the semiclassical calculation, respectively correspond to the above two types, and the former type plays the key role in the barrier tunnelling.

4.3. Characteristic branches around the critical point

$\mathcal{M}_\mathcal{S}$-set. Now, we investigate how the characteristic branches $\mathcal{M}_\mathcal{R}$ and $\mathcal{M}_\mathcal{C}$ appear in the close neighbourhood of the critical point, if the input and output boundary conditions are imposed on the trajectories. The input boundary condition was already used to obtain the

relation between α and $t_1 - t_{1c}$ (or $\mu_- - \mu_{-c}$) given by equation (41). We now impose the output boundary condition $E(t_2) = E_2$. We scan E_2 over the whole real range to obtain the set $\mathcal{M}_S$ of the contributing trajectories, which is achieved by putting $E_\infty = E_2$ in equation (54) and varying it along the real line:

$$E_2 = a(\mu_+)(1 - \alpha^2/\sqrt{2}) \in \mathbf{R}. \tag{60}$$

Hence, μ_+ has to satisfy the relation

$$\mathrm{Im}\left\{\epsilon \sin(\omega\mu_+) - \frac{\alpha^2}{\sqrt{2}}\right\} = 0. \tag{61}$$

Equation (60) shows that E_2 is explicitly represented as a function of μ_+ but not of t_1. However, E_2 must be a function of t_1 through μ_+, so that $\mathcal{M}_\mathcal{R}$ and $\mathcal{M}_\mathcal{C}$ are determined as the set of t_1 satisfying equation (61). First, from equation (44), the distance between μ_+ and μ_- is represented as a logarithmic function of α. Since $\mu_- - \mu_{-c} \sim O(\alpha^2/\epsilon\omega) \ll O(1)$ (see equations (41) and (42)), the entrance gate μ_- is well approximated by the gate μ_{-c} and μ_+ is rewritten as

$$\begin{aligned}\mu_+ &\sim \mu_{-c} + \tfrac{1}{\sqrt{2}}\{\log 2^{5/2} - \log\alpha^2 - \mathrm{i}n\pi\} \\ &= -\tfrac{1}{\sqrt{2}}\log\alpha^2 + C_R + \mathrm{i}C_I,\end{aligned} \tag{62}$$

where $C_R = \mathrm{Re}\,\mu_{-c} + \frac{1}{\sqrt{2}}\log 2^{5/2}$ and $C_I = \mathrm{Im}\,\mu_{-c} - \frac{1}{\sqrt{2}}n\pi$. Recalling that $\alpha^2 \propto t_1 - t_{1c}$ from equation (41), the parameter α^2 is identified with t_1, and we are able to see the structure of the branches $\mathcal{M}_\mathcal{R}$ and $\mathcal{M}_\mathcal{C}$ on α^2-plane instead of t_1-plane.

Equations (60) and (62) together with equation (41) provide basic relations which relate the output energy E_2 with the input condition $t_1 - t_{1c}$ and the smallness parameter α^2 characterizing the closeness of the trajectory to O. The relationship among E_2, t_1 and α^2 will be used frequently in the following arguments.

Relations (61) and (62) yield the equation for the branches $\mathcal{M}_\mathcal{R}$ and $\mathcal{M}_\mathcal{C}$:

$$\epsilon\cos\left(\omega\left(C_R - \frac{1}{\sqrt{2}}\log R\right)\right)\sinh\left(\omega\left(C_I - \frac{\theta}{\sqrt{2}}\right)\right) \sim \frac{R}{\sqrt{2}}\sin\theta, \tag{63}$$

where the polar coordinate (R, θ) on complex α^2-plane is introduced, i.e., $\alpha^2 = R\,\mathrm{e}^{\mathrm{i}\theta}$. In the limit $\alpha \to 0$, the condition in equation (63) is reduced to the two equations:

$$\cos\left(\omega\left(C_R - \frac{1}{\sqrt{2}}\log R\right)\right) \sim 0, \tag{64}$$

$$\sinh\left(\omega\left(C_I - \frac{\theta}{\sqrt{2}}\right)\right) \sim 0. \tag{65}$$

From these conditions, the branches $\mathcal{M}_\mathcal{R}$ and $\mathcal{M}_\mathcal{C}$ are respectively defined by

$$\mathcal{M}_\mathcal{R} = \{\alpha^2 | \theta = \theta_c \equiv \sqrt{2}C_I \text{ or } \theta = \theta_c + \pi\}, \tag{66}$$

$$\mathcal{M}_\mathcal{C} = \left\{\alpha^2 | R = R_m = \exp\left\{-\frac{\sqrt{2}}{\omega}\left(m + \frac{1}{2}\right)\pi + \sqrt{2}C_R\right\}\right\}. \tag{67}$$

α^2's that satisfy the former condition of equation (66) form a straight line passing through the origin of α^2-plane, namely t_{1c} on t_1-plane. This is the branch $\mathcal{M}_\mathcal{R}$. The latter condition (67) constructs a series of concentric circles with a common centre at the origin, which is nothing more than $\mathcal{M}_\mathcal{C}$ observed numerically. (Note that the integer m does not take a negative value

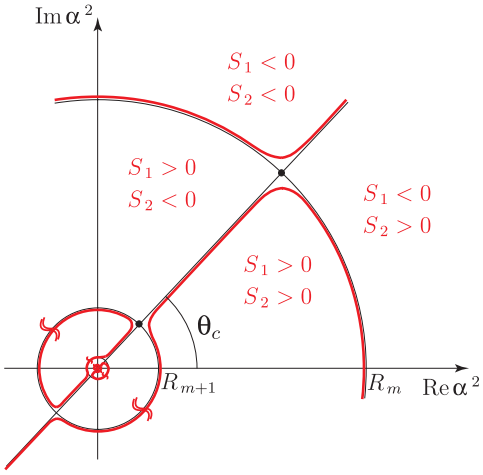

Figure 9. Sketch of branches in α^2-plane. The black thin lines and circles respectively indicate the branches $\mathcal{M}_{\mathcal{R}}$ and $\mathcal{M}_{\mathcal{C}}$ defined by equations (66) and (67). The red thick curves are actual branches given by equation (63) with non-zero α, where $S_1 = \cos(\omega(C_R - \frac{1}{\sqrt{2}}\log R))$ and $S_2 = \sinh(\omega(C_I - \frac{\theta}{\sqrt{2}}))$, and • indicates the caustic.

because $|R_m| \ll 1$ for $\omega \ll 1$; when $\mathrm{Re}\,\mu_{-c} \sim -\pi/2\omega$, R_0 corresponds to the radius of the outermost circle of figure 6(*a*).)

The latter condition (67) results in a series of concentric circles with a common centre at the origin, which is nothing more than $\mathcal{M}_{\mathcal{C}}$ observed numerically. The ratio of radii of two successive circles of $\mathcal{M}_{\mathcal{C}}$ is estimated by

$$R_{m+1}/R_m \sim \exp\{-\sqrt{2}T/2\}. \tag{68}$$

Note that from equation (61), $\mathrm{Im}\,\mu_+ \sim 0$ for $\mathcal{M}_{\mathcal{R}}$, while $\omega\,\mathrm{Re}\,\mu_+ \sim \left(m + \frac{1}{2}\right)\pi$ for $\mathcal{M}_{\mathcal{C}}$. The sets $\mathcal{M}_{\mathcal{R}}$ and $\mathcal{M}_{\mathcal{C}}$ are illustrated in figure 9.

The $\mathcal{M}_{\mathcal{S}}$-set is decomposed into the straight line ($\mathcal{M}_{\mathcal{R}}$) and the circles ($\mathcal{M}_{\mathcal{C}}$) only in the close neighbourhood of the origin, i.e., t_{1c}. Going far from t_{1c}, $|\alpha|$ becomes large, and the structure of the branches is deformed and finally they lose their characteristic shapes. Even if $|\alpha| \ll 1$, branches observed numerically are, as illustrated in figure 9, neither a circle nor a straight line in the close vicinity of their intersection (R_m, θ_c). Precisely speaking, they do not intersect but form a separated pair of branches. Such a tiny local deformation is actually reproduced by equation (63) if the small term of $O(\alpha^2)$ on the right-hand side of equation (63) is not neglected. Indeed, the separated pair close to (R_m, θ_c) is well approximated by the hyperbola:

$$(-1)^{m+1}(R - R_m)R_m(\theta - \theta_c) \sim \sqrt{2}\frac{R_m^2}{\epsilon\omega^2}R_m \sin\theta_c \sim O\left(\frac{\alpha^6}{\epsilon\omega^2}\right), \tag{69}$$

which have the circle $\mathcal{M}_{\mathcal{C}}$ and the line $\mathcal{M}_{\mathcal{R}}$ as their asymptotes, and there exists a caustic at the centre of the hyperbola as shown in figure 9. Such a structure of branches around a caustic is a typical form of complex domain branches [14, 17]. From equation (69), the gap between the pair of branches is of $O(\alpha^3/\sqrt{\epsilon\omega^2})$ and the ratio of it to the radius R_m is estimated as $O(\alpha/\sqrt{\epsilon\omega^2})$. Thus the gap between the branches is negligibly small if $|\alpha^2| \ll \epsilon\omega^2$, and out of this quite narrow region the branches can be regarded as the product set of $\mathcal{M}_{\mathcal{R}}$ and $\mathcal{M}_{\mathcal{C}}$.

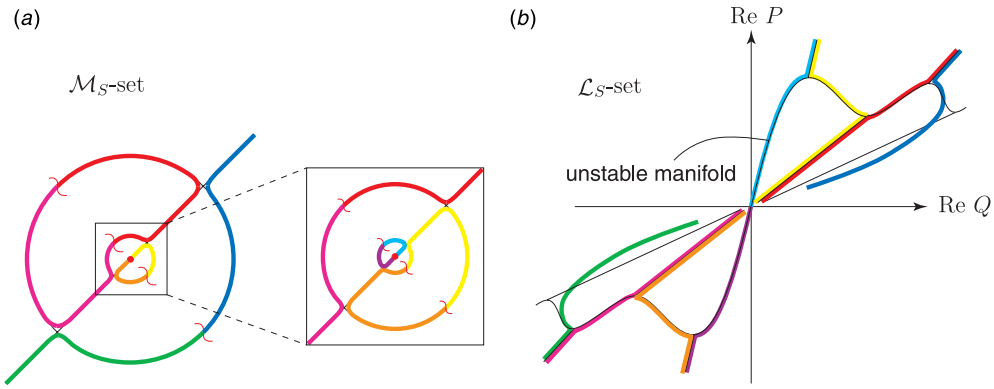

Figure 10. Correspondence between (*a*) $\mathcal{M}_S$-set and (*b*) $\mathcal{L}_S$-set. The same colour specifies the corresponding parts of $\mathcal{M}_S$-set and $\mathcal{L}_S$-set. In (*b*) the thin black curves, which closely overlap with coloured branches of $\mathcal{L}_S$-set, indicate $W_u(t)$: the wavy curve is $W_{uR}(t)$, while the straight lines are $W_u(t) - W_{uR}(t)$.

In our numerical calculation (see figure 6(*a*)), only the outermost circle can be detected. This is because, from equation (68), other circles inside it become exponentially small and cannot be calculated within the limit of numerical accuracy. Those inner circles can be ignored in the semiclassical calculation, because their contributions to the plateau spectrum are exponentially small due to the amplitude factor (16), which diminishes as $t_1 \to t_{1c}$. This will be discussed in section 4.4.

$\mathcal{L}_S$-set. Let us discuss the nature of $\mathcal{L}_S$-set corresponding to the characteristic branches $\mathcal{M}_\mathcal{R}$ and $\mathcal{M}_\mathcal{C}$. The trajectories starting at the branches defined by equation (63), i.e., $\mathcal{M}_\mathcal{R}$ and $\mathcal{M}_\mathcal{C}$, satisfy the output boundary condition of the S-matrix and take real values in the output energy E_2. As discussed in subsection 4.2, each trajectory specified by μ_+ is connected to a trajectory of μ_{+c} on W_u with the same output energy E_2, namely $a(\mu_{+c}) = E_2 \in \mathbf{R}$. We scan E_2 from 0 to $+\infty$, then the condition $a(\mu_{+c}) \in \mathbf{R}$ gives the two types of the gate μ_{+c}:

$$\mu_{+c}^R = \{\mu_{+c} | \mu_{+c} \in \mathbf{R}\} \qquad \text{for} \quad 1 - \epsilon \leqslant E_2 \leqslant 1 + \epsilon, \tag{70}$$

$$\mu_{+c}^C = \left\{\mu_{+c} | \mathrm{Re}\mu_{+c} = \left(m + \tfrac{1}{2}\right)\pi, \mathrm{Im}\,\mu_{+c} \neq 0\right\} \qquad \text{for} \quad E_2 < 1 - \epsilon \text{ or } E_2 > 1 + \epsilon. \tag{71}$$

At a given time t, the set of all the trajectories specified by μ_{+c} in μ_{+c}^R or μ_{+c}^C forms a slice of W_u, which we denote by $W_u(t)$. If we restrict μ_{+c} to $\mu_{+c} \in \mu_{+c}^R$, then all the trajectories make a slice of the real unstable manifold $W_{uR}(t)$, when t is fixed at a real value. On the other hand, for all the complex $\mu_{+c} \in \mu_{+c}^C$, the trajectories form a 1D subset in $W_u(t) - W_{uR}(t)$, which looks like whiskers emanating from the apexes and anti-apexes of the oscillating $W_{uR}(t)$ in the asymptotic region (see figure 10(*b*), in which $W_{uR}(t)$ accompanied by the whiskers is drawn by thin black lines). The whiskers further extend deeper into the imaginary plane. Figure 10 schematically illustrates the relation between the branch of $\mathcal{M}_\mathcal{R}$ or $\mathcal{M}_\mathcal{C}$ and the corresponding branch of $\mathcal{L}_\mathcal{S}$ at a given time $t \in \mathbf{R}$. Every part of branches on $\mathcal{M}_\mathcal{R}$ (figure 10 (*a*)) is mapped to a part of $\mathcal{L}_\mathcal{S}$ which lies very close to $W_{uR}(t)$ (figure 10(*b*)). Deviation of the branch of $\mathcal{L}_\mathcal{S}$ from $W_{uR}(t)$ becomes significant as it goes away from the origin, which is due to the increase in α^2's (see equation (58)). The parts of $\mathcal{L}_\mathcal{S}$ corresponding to the arc branches along $\mathcal{M}_\mathcal{C}$ follow the complex whiskers emanating from the turning points of $W_{uR}(t)$.

The line $\mathcal{M}_{\mathcal{R}}$ is divided into the two sections by t_{1c}, and the trajectories starting from different sections land on the opposite sides of the asymptotic region, i.e., the reflection or transmission side. The topological change of the integration path with respect to the singularities Sg_n^+, which was discussed in subsection 3.3, occurs as t_1 goes through t_{1c}. Cuts should, thus, take place along a line passing through t_{1c} and perpendicular to $\mathcal{M}_{\mathcal{R}}$, which divide a neighbourhood of t_{1c} into two areas: one contributing to the reflection sides and the other contributing to the transmission side. As a result, a circle of $\mathcal{M}_{\mathcal{C}}$ is composed of the two semicircles separated by the cuts, as was shown in figure 6(*a*). When a branch of $\mathcal{M}_{\mathcal{C}}$ is continued analytically across a cut, it goes to a different Riemann sheet. Such a topological anomaly of branches around t_{1c} should be understood in connection with the logarithmic divergence of the singularities Sg_n^+ at t_{1c} [18, 27].

4.4. Evaluation of spectral intensity

In this subsection, we analytically evaluate the spectral intensity of the S-matrix contributed by $\mathcal{M}_{\mathcal{R}}$ and $\mathcal{M}_{\mathcal{C}}$ obtained in the previous subsection. Since the contribution from the trajectory is mostly determined by the imaginary part of the classical action as $\sim \exp(-\mathrm{Im}\, S_S/\hbar)$, we first roughly estimate it.

An important relation comes from equation (15):

$$\mathrm{Im}\,\frac{\partial S_S(E_1, E_2)}{\partial E_2} = \mathrm{Im}\, t_2 \sim \mathrm{Im}\,\mu_+. \tag{72}$$

Recall that, from equations (60) and (62), μ_+ can be regarded as a function of the energy E_2 via the parametric variable $\alpha^2 = A_1(t_1 - t_{1c})$. The arguments in subsections 4.2 and 4.3 reveal that, when t_1 moves off from t_{1c} along the transmission or the reflection part of $\mathcal{M}_{\mathcal{R}}$, $\mathrm{Im}\,\mu_+$ takes a nearly zero value, which means that $\mathrm{Im}\, S_S(E_1, E_2)$ remains almost constant in the range of E_2 covered by the relevant branch. On the other hand, as t_1 is moved away from an intersection between $\mathcal{M}_{\mathcal{C}}$ and $\mathcal{M}_{\mathcal{R}}$ along the two paired branches of $\mathcal{M}_{\mathcal{C}}$, $|\mathrm{Im}\,\mu_+|$ increases, resulting in a rapid increase in $|\mathrm{Im}\, S_S(E_1, E_2(t_1))|$: along one branch, $\mathrm{Im}\,\mu_+$ increases in the positive direction and $\mathrm{e}^{-\mathrm{Im}\, S/\hbar}$ suffers an exponential drop-off; along the other branch, $\mathrm{Im}\,\mu_+$ increases in the negative direction, which gives rise to an exponential increase of the weight, and it is removed as an unphysical contribution due to the Stokes phenomenon [15, 17].

Hence, the branch $\mathcal{M}_{\mathcal{R}}$ makes a major contribution to the spectral intensity, and so we concentrate our attention on it. To evaluate the action $S_S(E_1, E_2)$, we here adopt a more precise approximation than in the previous subsections. This is because we would like to discuss later the dependence of $\mathrm{Im}\, S_S(E_1, E_2)$ upon $t_1 (\in \mathcal{M}_{\mathcal{R}})$ instead of E_2. First, the classical action S_S of equation (14) is rewritten as

$$S_S(Q_2, E_2, Q_1, E_1) = \int_{t_1}^{t_2} \{H(Q, P, \omega t) - 2V(Q, \omega t)\}\,\mathrm{d}t + E_2 t_2 - E_1 t_1, \tag{73}$$

where $V(Q, \omega t) \equiv V_0(Q) + \epsilon v_1(Q, \omega t)$. The integral

$$\int_{t_1}^{t_2} V(Q(t), \omega t)\,\mathrm{d}t = \int_{t_1}^{t_2} \frac{a(t)}{\cosh^2 \mathrm{Q(t)}}\,\mathrm{d}t \tag{74}$$

can be evaluated by substituting the unperturbed solution (23) into $Q(t)$ and after a long manipulation, which is outlined in appendix A, we get a very simple result,

$$\int_{t_1}^{t_2} V(Q(t), \omega t)\,\mathrm{d}t \sim \left(1 - \frac{\lambda^2}{2}\right) \int_{\mu_-}^{\mu_+} a(t)\,\mathrm{d}t, \tag{75}$$

where $\lambda = \alpha/(2E_{10})^{1/4}$ and E_{10} denotes the energy of the unperturbed solution given as a solution of $\alpha^2/\sqrt{2E_{10}} = 1/E_{10} - 1$.

Next we estimate the energy integral $\int_{t_1}^{t_2} H(Q(t), P(t), t))\,\mathrm{d}t = \int_{t_1}^{t_2} E(t)\,\mathrm{d}t$ in equation (73). Since $E(t)$ itself is computed by integrating the energy gain equation (32), the energy integral is given as a double integral over t, and some careful treatment is required for the evaluation of $E(t)$. We compute $E(t)$ up to the correction of $O(\epsilon\omega)$ according to the outline stated in appendix A:

$$E(t) \sim \begin{cases} a(\mu_-)\left(1 - \dfrac{\alpha^2}{\sqrt{2a(\mu_-)}}\right) + \dfrac{\dot{a}(t)}{2\sqrt{2E_{10}}} \log(1 + \mathrm{e}^{2\sqrt{2E_{10}}(t-\mu_-)}) & (\text{if } \mathrm{Re}\, t < \mathrm{Re}\, \mu_-) \\ a(t)\left(1 - \dfrac{\alpha^2}{\sqrt{2a(t)}}\right) + \dfrac{\dot{a}(t)}{2\sqrt{2E_{10}}} \log(1 + \mathrm{e}^{-2\sqrt{2E_{10}}(t-\mu_-)}) & (\text{if } \mathrm{Re}\, \mu_- < \mathrm{Re}\, t < \mathrm{Re}\, t_0) \\ a(t)\left(1 - \dfrac{\alpha^2}{\sqrt{2a(t)}}\right) - \dfrac{\dot{a}(t)}{2\sqrt{2E_{10}}} \log(1 + \mathrm{e}^{2\sqrt{2E_{10}}(t-\mu_+)}) & (\text{if } \mathrm{Re}\, t_0 < \mathrm{Re}\, t < \mathrm{Re}\, \mu_+) \\ a(\mu_+)\left(1 - \dfrac{\alpha^2}{\sqrt{2a(\mu_+)}}\right) - \dfrac{\dot{a}(t)}{2\sqrt{2E_{10}}} \log(1 + \mathrm{e}^{-2\sqrt{2E_{10}}(t-\mu_+)}) & (\text{if } \mathrm{Re}\, t > \mathrm{Re}\, \mu_+). \end{cases} \tag{76}$$

This provides an improved version of equation (35), where the input and output energies are respectively given by

$$E_1 = a(\mu_-)(1 - \alpha^2/\sqrt{2a(\mu_-)}), \tag{77}$$

$$E_2 = a(\mu_+)(1 - \alpha^2/\sqrt{2a(\mu_+)}). \tag{78}$$

By using equation (76) together with equations (77) and (78), the integral of E over t is achieved leaving a resultant expression

$$\int_{t_1}^{t_2} H(Q(t), P(t), \omega t)\,\mathrm{d}t \sim \int_{\mu_-}^{\mu_+} a(t)\left(1 - \frac{\alpha^2}{\sqrt{2a(t)}}\right)\mathrm{d}t + (\mu_- - t_1)E_1 + (t_2 - \mu_+)E_2 + \frac{\dot{a}(\mu_-)}{4E_{10}}\frac{\pi^2}{12} - \frac{\dot{a}(\mu_+)}{4E_{10}}\frac{\pi^2}{12}. \tag{79}$$

Substitution of equations (75) and (79) into equation (73) gives the final expression of S_S,

$$S_S(Q_2, E_2, Q_1, E_1) = \frac{\epsilon}{\omega}(\cos\omega\mu_+ - \cos\omega\mu_-) + 2E_1(\mu_- - t_1) + 2E_2(t_2 - \mu_+) - \mu_-(E_1 - 1) + \mu_+(E_2 - 1) + \int_{\mu_-}^{\mu_+}\left(\frac{\alpha^2}{\sqrt{2E_{10}}} - \frac{\alpha^2}{\sqrt{2a(t)}}\right)a(t)\,\mathrm{d}t + \frac{\dot{a}(\mu_-)}{4E_{10}}\frac{\pi^2}{12} - \frac{\dot{a}(\mu_+)}{4E_{10}}\frac{\pi^2}{12}. \tag{80}$$

Here we take the boundary condition $\mathrm{Im}\, E_1 = \mathrm{Im}\, E_2 = 0$ into account. In particular, we are interested in the action along the critical trajectory which starts at $t_1 = t_{1c}$, because it is the key parameter characterizing the intensity of the plateau spectrum, which is contributed by the branch $\mathcal{M}_{\mathcal{R}}$. Taking the limit $\alpha^2 \to 0$ and using $\mathrm{Im}\, t_2 = \mathrm{Im}\, \mu_+ = 0$, we obtain the imaginary action along the critical trajectory:

$$\mathrm{Im}\, S_{Sc}(Q_2, E_2, Q_1, E_1) \sim -\frac{\epsilon}{\omega}\mathrm{Im}\cos\omega\mu_{-c} - \mathrm{Im}\,\mu_{-c}(E_1 - 1). \tag{81}$$

Let us compare the analytical evaluation of equation (81) with the numerical result. Substituting $\epsilon = 0.4, \omega = 0.3$ and $E_1 = 0.5$ into equation (81), and using the estimation for $\mathrm{Im}\,\mu_{-c} \sim \mathrm{Im}\, t_{1c}$ given by equation (25), S_{Sc} is estimated to be ~ 0.154, which shows a fairly good agreement with the numerical value $\mathrm{Im}\, S_{Sc} \sim 0.192$.

Im S_S of trajectories at t_1 very close to t_{1c} is well approximated by equation (81). However, as t_1 moves away from t_{1c} along $\mathcal{M}_\mathcal{R}$, Im S_S varies slowly, because Im $\partial S_S/\partial E_2 = \text{Im}\, t_2$ has small but non-zero values. Taking higher order terms into account (see appendix B for details), we can estimate the slight variation of Im S_S as a function of $\delta t_1 \equiv t_1 - t_{1c}$,

$$\text{Im}\,\Delta S_S \equiv \text{Im}\, S_S(t_1) - \text{Im}\, S_S(t_{1c}) \sim D_1\epsilon\omega^2|\delta t_1| + D_2\epsilon\omega^2|\delta t_1|^2, \tag{82}$$

where D_1 and D_2 are constants of $O(1)$. Unfortunately, we do not succeed in the numerical evaluation of D_1 and D_2, but we can conjecture the signs of the constants so as to be consistent with the numerical semiclassical results. They tell that Im S_S increases very slowly as t_1 moves from t_{1c} along the red line of $\mathcal{M}_\mathcal{R}$ in figure 6(*a*). A significant increase begins beyond a certain characteristic distance. To be consistent with this observation, we may conjecture that $D_1 > 0$ and $D_2 > 0$. The above-mentioned characteristic value of $|\delta t_1|$ beyond which S_S significantly increases from S_{Sc} and hence a marked decrease of the quantum weight $\sim e^{-S_S/\hbar}$ is observed is roughly estimated by

$$\delta t_{1,\max} \equiv \frac{1}{\omega}\min\{\hbar/\epsilon\omega, \sqrt{\hbar/\epsilon}\}. \tag{83}$$

The part of $\mathcal{M}_\mathcal{R}$ in the range $|\delta t_1| < \delta t_{1,\max}$ actually contributes to forming the plateau of the tunnelling spectrum.

In the above argument we do not take into account the amplitude factor. However, when t_1 comes very close to t_{1c}, the amplitude factor of the semiclassical S-matrix (16) becomes dominant in the evaluation of the probability weight: as t_1 comes closer to t_{1c}, the trajectory leaving at t_1 passes closer to the unstable saddle O, spending longer time in the scattering region, which results in an exponentially small amplitude factor because of the exponential instability.

Evaluation of the amplitude factor (16) is done by calculating the partial derivative of E_2 with respect to t_1, i.e., $\partial E_2/\partial t_1$, within the approximation described above. Indeed, as mentioned in section 4.3, E_2 is expressed as a function of t_1 and we are able to evaluate the derivative $\partial E_2/\partial t_1$ (see appendix C), arriving at the expression of the amplitude factor:

$$\begin{aligned} Amp(t_1) = \sqrt{\frac{\partial^2 S_S}{\partial E_1 \partial E_2}} &\sim \left(\left(\frac{1}{\sqrt{2}\delta t_1} - 1\right)\dot{a}(\mu_+) + \frac{A_1}{2}\sqrt{2a(\mu_+)}\right)^{-1/2} \\ &\sim \begin{cases} \sqrt{\dfrac{\sqrt{2}}{\dot{a}(\mu_+)}\delta t_1} \sim O\left(\dfrac{\alpha}{\epsilon\omega}\right) & (\text{if} \quad |\delta t_1| \ll 1) \\ O\left(\sqrt{\dfrac{1}{\epsilon\omega}}\right) & (\text{if} \quad |\delta t_1| \gg 1). \end{cases} \end{aligned} \tag{84}$$

Thus $Amp(t_1)$ is proportional to $\sqrt{\delta t_1}$ in the limit $t_1 \to t_{1c}$.

Figure 10(*a*) indicates that, in the close neighbourhood of t_{1c}, an infinite number of similar branches of $\mathcal{M}_S$, each of which consists of circular and radial components, accumulate. As shown in equation (68), the inner branch is exponentially smaller in radius measured from t_{1c} than the outer branch. Therefore, the amplitude factor $Amp(t_{1,m})$ of the mth inner branch decreases exponentially with m from equations (68) and (84), and their contributions are negligibly small as compared to that of the outermost branch, namely,

$$Amp(t_{1,m})/Amp(t_{1,m=0}) = \exp\{-\sqrt{2}Tm/4\}. \tag{85}$$

Combining equations (81), (82) and (84), the spectral intensity contributed by $\mathcal{M}_\mathcal{R}$ is

$$W(\delta t_1) \sim \frac{C_1\sqrt{|\delta t_1|}}{\sqrt{\epsilon\omega}} \exp\left\{-\frac{1}{\hbar}(\text{Im}\, S_S(t_{1c}) + D_1\epsilon\omega^2|\delta t_1| + D_2\epsilon\omega^2|\delta t_1|^2)\right\}, \tag{86}$$

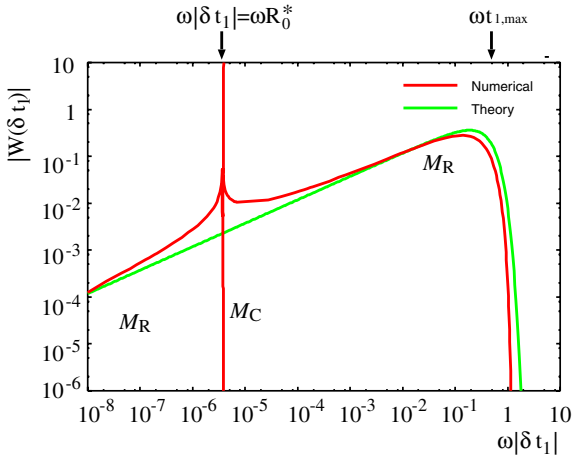

Figure 11. The weight of $\mathcal{M}_{\mathcal{R}}$ as a function of $\omega|\delta t_1|$. The theoretical prediction given by equation (86) (green) with $C_1 = D_1 = D_2 = 1$ is compared with the numerical result (red).

where C_1, D_1 and D_2 are positive real numbers of $O(1)$. Figure 11 shows the numerically computed semiclassical probability weight contributed by the branch $\mathcal{M}_{\mathcal{R}}$ (in figure 6(*a*)) as a function of δt_1, which is compared with the analytical prediction (86). Here the unknown parameters are taken as $C_1 = D_1 = D_2 = 1$. Our result well captures the essential feature of the probability weight obtained numerically. In the numerical result, the divergence close to the vertical line at $|\delta t_1| = R_0^*$ is an artifact due to the caustic, which is inevitable in the semiclassical treatment. As mentioned above, the inner part $|\delta t_1| < R_0^*$ does not make a dominant contribution due to its exponentially smaller amplitude factor, so the major contribution to the plateau comes from the part $R_0^* < |\delta t_1| < \delta t_{1,\max}$. In fact, this dominant contributing part forms most of the plateau, if the variable δt_1 rewritten in terms of the observed energy E_2, using relations (60), (62) and (41) (for an intuitive view see figures 6(*a*) and 7(*a*) compared with figure 11).

In conclusion, the plateau is formed by the tunnelling trajectories which are launched at the outermost branch of $\mathcal{M}_{\mathcal{R}}$ in the close neighbourhood of the critical point. They are guided by the complexified W_s and finally land close to the real phase space following the real W_u. The broad support of the plateau spectrum is the reflection of W_u stretched in the momentum direction as illustrated in figure 6(*b*).

5. Discussion and summary

5.1. Return to the autonomous model

Before summarizing this paper, we interpret our results for the periodically perturbed model in terms of the original 2D autonomous model. As in section 2.1, we consider an energy shell with a fixed total energy E_{tot}. Instead of the Poincaré surface of section Σ shown in figure 1, we, for convenience of discussion, consider a different Poincaré surface of section Σ_Q, which is taken at every fixed Q (and so is defined in the channel coordinate (q, p)). If Q is fixed at $Q = Q_1 \gg 1$ in the asymptotic region of the reactant side, the initial manifold $\mathcal{I}$ with the given reaction energy $P_1^2/2$ forms an ellipse $h_e = \{(q, p)|p^2/2 + \omega^2 q^2/2 = e_{ch}\}$ with the channel energy (or action) $e_{ch} = I_1\omega = E_{\text{tot}} - P_1^2/2$ on the section Σ_{Q_1}. On the other hand,

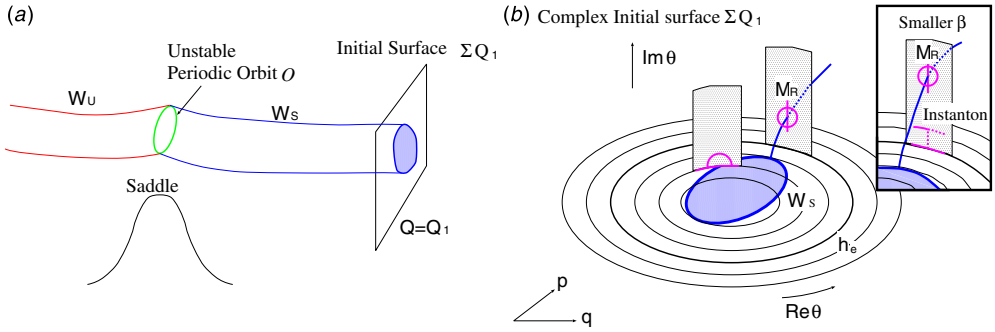

Figure 12. (*a*) Schematic illustration of the unstable periodic orbit O accompanied by the tubes formed by W_s and W_c. (*b*) Intersections of $\mathcal{I}$ and W_s on Σ_{Q_1} at various values of e_{ch}, and the set $\mathcal{M}_{\mathcal{R}}$ and $\mathcal{M}_{\mathcal{C}}$ on $\mathcal{I}$. The inset box shows the case for a smaller value of coupling constant β.

the angle variable $\theta = \arctan(\omega q/p)$ specifying a point on the ellipse should be read as the initial time t_1 by the relation $\theta = \omega t$ (see equation (10)). The intersection between the real W_s and Σ_{Q_1} forms a closed curve on Σ_{Q_1} as shown in figure 12(*a*). Varying Q from Q_1 to the origin, the intersection of W_s forms a tube which approaches the unstable periodic orbit O, from which the tube of W_u extended into the product side is emanating, as illustrated in figure 12(*a*).

Note that the intersections of W_s with h_e are, if they occur on the real plane, nothing more than the critical points emerging in the real phase space, which correspond to the intersections of W_s and $\mathcal{I}_a$ displayed in figure 1. The real classical trajectories from the inside of W_s can go over the barrier, whereas those from the outside are all reflected by the barrier. Thus the real initial manifold represented by the ellipse h_e whose energy e is larger than the critical energy $\mathrm{e}^{\max} = E_{\mathrm{tot}} - P_{\min}^2/2$ has no real trajectories going across the barrier, and only the complexified trajectories emanating from the complexified h_e can go over the barrier. Extension of h_e into the complex domain is achieved by complexifying the angle variable $\theta = \arctan(\omega q/p)$ keeping e at a fixed real number and, as is depicted in figure 12(*b*), there emerge complex critical points at the intersections between the complexified W_s and h_e, which appear as a complex conjugate pair at $\theta = \theta_c(e_{ch})$ and $\theta = \theta_c^*(e_{ch})$. Note that one of the critical points, e.g. $\theta_c^*(e_{ch})$, making an unphysical contribution is discarded in the semiclassical calculation with the proper treatment of the Stokes phenomenon [26]. In the close vicinity of the critical point θ_c, the set $\mathcal{M}_{\mathcal{R}}$, which plays the major role in the tunnelling process, exists. The trajectories from it end up being along $W_u \cap \mathbf{R}^2$ on Σ_Q on the product side and contribute to forming the broad plateau in the tunnelling spectrum.

However, as shown in the inset box in figure 12(*b*), for a smaller value of coupling constant β, the critical point shifts deeper into the imaginary plane and so does $\mathcal{M}_{\mathcal{R}}$, which means that the actions along the trajectories from $\mathcal{M}_{\mathcal{R}}$ gain larger imaginary parts and contribute less to the S-matrix. Instead, the instanton branches, which appear on the lower imaginary side of the complexified h_e, become the major carrier of tunnelling probability. The change of the tunnelling spectrum shown by figure 2 in the order of (c)→(b)→(a) indicates the change of the underlying classical mechanism making the major tunnelling contribution, from the new tunnelling mechanism to the instanton mechanism.

In the case that β is fixed but e_{ch} is increased (i.e., h_e is replaced by a larger ellipse), $\theta_c(e_{ch})$ moves deeper into the imaginary plane, and the depth of the instanton branch in the imaginary plane, which is estimated by a half period of the instanton orbit for the unperturbed potential $V_0(Q)$, also increases with e_{ch}. Thus, without quantitative analysis, we cannot make a definite

claim as to which of the two mechanisms dominates the tunnelling process. A detailed study of this problem is beyond the scope of this paper and will be published elsewhere [27].

Recently, Creagh and coworkers developed a semiclassical theory of multi-dimensional tunnelling, in a situation similar to the situation considered in this paper, by introducing the reaction operator, which is convenient for visualizing the transmission probability on Σ_Q by using the Weyl symbol [12]. Their semiclassical formalism taking account of the contribution to tunnelling from the outside of the tube W_s seems to well reproduce the fully quantum results, although their tunnelling trajectories relevant for the reaction operator formula are not the same as those we treated in this paper. Whether or not the tunnelling mechanism discussed in our papers plays any role in their results is not yet clear. According to the spirit of the reaction operator, contributions from all the initial states of the channel at a given total energy $E_{\rm tot}$ are summed up and so the contributions from the branches $\mathcal{M}_{\mathcal{R}}$ may be concealed by the averaging effect and/or by the ambiguity inherent in the phase-space representation of the quantum state. We strongly hope that their approach and ours can be reconciled to better elucidate an entire view of multi-dimensional barrier tunnelling.

5.2. Summary

In this paper, we have elucidated a key feature of the new universal mechanism for tunnelling which has been recently proposed in [18]. In this new tunnelling mechanism complex-classical trajectories are guided by the stable–unstable manifolds emanating from the dividing unstable periodic orbit above the top of the potential barrier, which has been recently termed the normally hyperbolic invariant manifold (NHIM) [29–31]. We have demonstrated numerically and theoretically that this tunnelling mechanism causes a characteristic plateau structure in the tunnelling spectrum.

Firstly, using an autonomous two-dimensional model of a barrier tunnelling system, we showed that the tunnelling spectrum computed by a fully quantum method has a characteristic plateau structure in the regime of strong coupling between the two degrees of freedom. We also confirmed that the spectrum of the 2D system is reproduced in a simpler model with a periodic perturbation. This simpler model is suited to detailed analysis of the tunnelling mechanism and the corresponding spectrum feature.

Secondly, the complex-domain semiclassical theory for the S-matrix is applied, and it was confirmed numerically that complex classical trajectories guided by the stable–unstable manifolds reproduce very well the plateau structure observed in the fully quantum tunnelling spectrum.

Thirdly, a detailed theoretical analysis based on the complex-classical solution, which is applicable in the low-frequency regime, has been developed to describe analytically the formation of the plateau spectrum. The following important points were elucidated by the theoretical analysis.

(1) The complexified stable manifold W_s emanating from the unstable saddle located on top of the potential always intersects with the initial manifold of the scattering problem $\mathcal{I}$ at any perturbation strength. The intersection points t_{1c}'s are called critical points.

(2) Trajectories starting in a neighbourhood close to the critical points t_{1c} are initially guided by W_s and eventually approach the unstable manifold W_u. Since W_u has a real component W_{uR}, the above fact means that in the vicinity of every critical point there is a set $\mathcal{M}_{\mathcal{R}}$ of initial conditions of trajectories which eventually approach very rapidly the real plane and land on the set $\mathcal{L}_{\mathcal{R}}$, which is located very close to W_u. Because of their rapid approach to the real plane these trajectories make dominant contributions to the spectrum.

(3) The trajectories which land close to W_{uR} contribute equally to the spectrum because the variation rate of action with respect to the output energy, which is just the arrival time, has a very small imaginary part (equation (72)). This is the very reason why the spectrum has a plateau.

The tunnelling mechanism described in the first point was reported previously in [18], but it is elucidated analytically in detail for the first time in this paper. Together, the above points constitute a scenario for manifestation of the plateau feature in the tunnelling spectrum.

The key mechanism of the above scenario is that there exist dominantly contributing tunnelling trajectories which are first guided by the complexified stable manifold and finally land close to the real plane following the real unstable manifold. This tunnelling mechanism is not peculiar to our system but is universal and occurs in more complicated systems, and so the scenario for the manifestation of the plateau structure in the tunnelling spectrum should also be universal and can be expected to be observed in physical experiments of reactive scattering systems.

How does the new mechanism appear in more realistic situations? A comprehensive answer to this question is left to future investigations. However, let us finally comment here on the issue of theoretically investigating more complicated reactive systems. The model used in this paper is a minimal model of multi-dimensional barrier tunnelling; the system has only one channel degree of freedom, and the transition state has only a single unstable saddle. In more realistic systems the reaction path may be curved, the number of channel degrees of freedom may be more than one, and there may be more than one saddle in the transition state.

The system studied in this paper is not complex enough to allow the existence of chaos, and so it cannot be used to study the complicated tunnelling phenomena in the presence of chaos in the real phase space. Time singularities generic in the complexified trajectories of continuous-time systems, make the analysis difficult for multi-dimensional continuous-time systems. However, it has been shown that the tunnelling mechanism described in this paper also operates in more complicated situations [16].

Map systems are advantageous for studying multi-dimensional tunnelling because they are time-discretized and are free from complications due to the time singularities generic in continuous-time systems, and so they are applicable to the study of complicated dynamics including chaos. Indeed, the complicated nature of chaotic tunnelling exhibited by quantum maps can be understood in terms of the complexified stable–unstable manifolds of saddles which are dense in chaotic invariant sets. Moreover, it has been shown that stable and unstable manifolds are dense in forward and backward Julia sets, respectively [32]. This implies that Julia sets control chaotic tunnelling [16].

However, as a result of the discretization, the perturbation by other degrees of freedom is non-analytic in map systems, and it has not been clarified whether they truly capture the features of the complex phase space of natural systems with analytic interactions. In fact divergence of the time singularities is closely related to the existence of the trajectories responsible for the new tunnelling mechanism of our system. Such a relationship is hidden and invisible in the analysis of the map systems. Nevertheless, it should be emphasized that in spite of apparent differences between the theoretical descriptions for the continuous-time system and the map system, the resulting physical mechanisms are very similar in both types of systems.

We further add the remark that the divergence of singularities is even more fundamental than the existence of W_s and W_u for understanding the complicated process of tunnelling in multi-dimensional systems. Indeed, even in systems with no saddles, divergence of the singularities may occur, leading to a tunnelling mechanism similar to the one demonstrated in this paper [20].

Acknowledgments

The authors are grateful to A Shudo and T Onishi for discussions and collaboration on related work. One of the authors (KT) thanks S C Creagh for useful discussions. We are also thankful to S Tsuji for allowing us to use freely his country house as a laboratory for our collaboration project. Figures 9 and 10 were drawn by R Shiromoto. The present work is supported by Grant-in-Aid for Scientific Research (C) No. 13640410, from Japan Society for the Promotion of Science (JSPA) and Grant-in-Aid for Scientific Research on Priority Areas(2) Nos. 14077220 and 16032210 from Ministry of Education, Culture, Sports, Science and Technology.

Appendix A. Melnikov-like evaluation for the potential integral and the time-dependent total energy

In this appendix, we will show how to evaluate the potential integral and the time-dependent total energy necessary for the calculation of the classical action S_S, which was discussed in section 4.4. As shown in [18], the Melnikov method applied to integration of the energy gain equation has an exact solution for the case of trajectories with $\alpha = 0$, i.e., trajectories on W_s (or W_u). However, for the case of $\alpha \neq 0$, the Melnikov integral is not calculated exactly and we have to rely on approximation to execute the integral.

First, we explain the general idea of our approximation. For the case of $\alpha \neq 0$, the time origin of the integral should be taken at $t = t_0$, at which the phase ϕ is set at null, $\phi(t_0) = 0$ (see equation (37)). From the formation of the solution, t_0 converges, in the limit $\epsilon \to 0$, to the time at which the unperturbed trajectory hits its turning point. The solution is identified by the two parameters t_0 and α: t_0 decides the relative phase of the external force to it and α determines the amount of separation from the saddle O. The energy E_α in the linearized region is given by

$$E_\alpha(t) = a(t)/(1 + \alpha^2/\sqrt{2E_\alpha(t)}) \sim a(t)(1 - \alpha^2/\sqrt{2a(t)}). \tag{A.1}$$

It is confirmed as follows: in the linearized region, the approximation, $Q \sim Y = r(t)\cosh\phi(t)$ and $P \sim \dot{Y}$, is justified, then substituting these into the Hamiltonian (11) and using equation (37) yield the expression of the energy (A.1).

According to the spirit of the Melnikov's perturbation theory, the solution $Q(t)$ in the integral under consideration is replaced by the unperturbed solution (23). Then the differences between t_0 and $\mu_\mp$ are also replaced by those for the unperturbed solution, respectively:

$$\mu_\mp - t_0 = \mp \sinh^{-1}(1/\lambda)/\sqrt{2E_{10}} \sim \mp(\log(1/\lambda) + \log(2 + \lambda^2/2))/\sqrt{2E_{10}}, \tag{A.2}$$

where $\lambda^2 = \alpha^2/\sqrt{2E_{10}}$ is a small parameter and E_{10}, which is the energy of the unperturbed solution, is given by taking the limit $\epsilon \to 0$ for equation (A.1), i.e., $E_{10} = 1/(1+\alpha^2/\sqrt{2E_{10}})$.

Let us first evaluate the integral of V given by equation (74), because it is simpler than the integration of the energy gain equation. According to our procedure explained above, it is separated into two parts divided at $t = t_0$:

$$\int_{t_1}^{t_2} \mathrm{d}s \frac{a(s)}{\cosh^2 Q} = -\int_{t_0}^{t_1} \mathrm{d}s \frac{a(s)}{\cosh^2 Q} + \int_{t_0}^{t_2} \mathrm{d}s \frac{a(s)}{\cosh^2 Q}, \tag{A.3}$$

where $Q(t)$ is replaced by the unperturbed solution (23). We confine ourselves to the former half process in the time regime $\mathrm{Re}\, t < \mathrm{Re}\, t_0$, since the latter half process can be treated

symmetrically. Under the assumption $|\alpha| \ll 1$, we can expand the integral of V from t_0 to t_1 up to the correction of $O(\alpha^2)$ as

$$\int_{t_0}^{t_1} \mathrm{d}s \frac{a(s)}{\cosh^2 Q} \sim \int_0^{t_1-t_0} \mathrm{d}\tau \left\{ \frac{a(t_0+\tau)}{1+\frac{\lambda^2}{4}\,\mathrm{e}^{-2\sqrt{2E_{10}}\tau}} \right\} \tag{A.4}$$

$$- \int_0^{t_1-t_0} \mathrm{d}\tau \left\{ \frac{\lambda^2 a(t_0+\tau)}{2\left(1+\frac{\lambda^2}{4}\,\mathrm{e}^{-2\sqrt{2E_{10}}\tau}\right)^2} \right\} \tag{A.5}$$

$$- \int_0^{t_1-t_0} \mathrm{d}\tau \left\{ \frac{\lambda^2 a(t_0+\tau)\,\mathrm{e}^{2\sqrt{2E_{10}}\tau}}{4\left(1+\frac{\lambda^2}{4}\,\mathrm{e}^{-2\sqrt{2E_{10}}\tau}\right)^2} \right\}. \tag{A.6}$$

On the other hand, as mentioned in subsection 4.1, the perturbation effectively works only in the scattering region, $\mathrm{Re}\,\mu_- < \mathrm{Re}\,t < \mathrm{Re}\,\mu_+$, namely $V_0 = 1/\cosh Q(t) \sim 1$ for the scattering region and $V_0 \sim 0$ for the asymptotic region, so the integral is roughly estimated as

$$-\int_{t_0}^{t_1} \mathrm{d}s \frac{a(s)}{\cosh^2 Q} = -\int_{t_0}^{\mu_-} \mathrm{d}s\, a(s) + \text{small corrections}. \tag{A.7}$$

Therefore, it is natural to evaluate the integral separately in the scattering region and the asymptotic region, i.e., $\int_{t_0}^{t_1} = \int_{t_0}^{\mu_-} \mathrm{ds} + \int_{\mu_-}^{t_0} \mathrm{ds}$. Actually, this separation of the integral allows the use of a sort of adiabatic approximation as shown below. Let us evaluate each term on the RHS of the above equation. The integral of equation (A.4) is, for example, rewritten after change of variables as

$$\text{equation (A.4)} = \int_{t_0}^{\mu_-} \mathrm{d}s\, a(s) + \int_0^{t_0-\mu_-} \mathrm{d}\tau' \left\{ \frac{a(\mu_-+\tau')}{1+\left(1-\frac{\lambda^2}{2}\right)\mathrm{e}^{2\sqrt{2E_{10}}\tau'}} \right\}$$
$$+ \int_0^{t_1-\mu_-} \mathrm{d}\tau' \left\{ \frac{a(\mu_-+\tau')}{1+\left(1+\frac{\lambda^2}{2}\right)\mathrm{e}^{-2\sqrt{2E_{10}}\tau'}} \right\}. \tag{A.8}$$

In the second and third terms on the RHS of equation (A.8), the time origin is shifted from t_0 to μ_- for convenience of expression and their integrands exhibit exponentially damped oscillations in forward and backward time evolutions, respectively. Therefore, under the assumption $\omega \ll 1$ the adiabatic approximation is used for evaluation of those integrals. Namely, the second term is further reduced as $\int_0^{t_0-\mu_-} \mathrm{d}\tau' = \int_0^{\infty} \mathrm{d}\tau' - \int_{t_0-\mu_-}^{\infty} \mathrm{d}\tau'$ and the lowest adiabatic approximation is applied to get the following expression:

$$\int_0^{t_0-\mu_-} \mathrm{d}\tau' \left\{ \frac{a(\mu_-+\tau')}{1+\left(1-\frac{\lambda^2}{2}\right)\mathrm{e}^{2\sqrt{2E_{10}}\tau'}} \right\} = -\int_0^{\infty} \mathrm{d}\tau \left\{ \frac{a(t_0+\tau)}{1+\frac{4}{\lambda^2}\,\mathrm{e}^{2\sqrt{2E_{10}}\tau}} \right\}$$
$$+ \int_0^{\infty} \mathrm{d}\tau' \left\{ \frac{a(\mu_-+\tau')}{1+\left(1-\frac{\lambda^2}{2}\right)\mathrm{e}^{2\sqrt{2E_{10}}\tau'}} \right\} \sim -a(t_0) \int_0^{\infty} \mathrm{d}\tau \left\{ \frac{1}{1+\frac{4}{\lambda^2}\,\mathrm{e}^{2\sqrt{2E_{10}}\tau}} \right\}$$
$$+ a(\mu_-) \int_0^{\infty} \mathrm{d}\tau' \left\{ \frac{1}{1+\left(1-\frac{\lambda^2}{2}\right)\mathrm{e}^{2\sqrt{2E_{10}}\tau'}} \right\}. \tag{A.9}$$

Making use of the equality $\int_0^{\infty} 1/(1+\beta\,\mathrm{e}^{\alpha x})\,\mathrm{d}x = (1/\alpha)\log(1+1/\beta)$ leaves us with

$$\int_0^{t_0-\mu_-} \mathrm{d}\tau' \left\{ \frac{a(\mu_-+\tau')}{1+\left(1-\frac{\lambda^2}{2}\right)\mathrm{e}^{2\sqrt{2E_{10}}\tau'}} \right\} \sim -\frac{a(t_0)}{2\sqrt{2E_{10}}} \log\left(1+\frac{\lambda^2}{4}\right) + \frac{a(\mu_-)}{2\sqrt{2E_{10}}} \log\left(2+\frac{\lambda^2}{2}\right). \tag{A.10}$$

Taking the limit $\mathrm{Re}\, t_1 \to -\infty$ and using the same adiabatic approximation also reduces the last term on the RHS of equation (A.8) to

$$\int_0^{t_1-\mu_-} \mathrm{d}\tau' \left\{ \frac{a(\mu_- + \tau')}{1 + \left(1 + \frac{\lambda^2}{2}\right) \mathrm{e}^{-2\sqrt{2E_{10}}\tau'}} \right\} \sim -\frac{a(\mu_-)}{2\sqrt{2E_{10}}} \log\left(2 - \frac{\lambda^2}{2}\right). \tag{A.11}$$

Within the approximation up to $O(\lambda^2)$, equation (A.4) is therefore estimated as

$$\text{equation (A.4)} \sim \int_{t_0}^{\mu_-} a(s)\, \mathrm{d}s + \frac{\lambda^2}{4\sqrt{2E_{10}}} a(\mu_-) - \frac{\lambda^2}{8\sqrt{2E_{10}}} a(t_0). \tag{A.12}$$

In the same way, equation (A.5) is reduced to

$$\text{equation (A.5)} \sim -\frac{\lambda^2}{2} \int_{t_0}^{\mu_-} a(s)\, \mathrm{d}s - \frac{\lambda^2}{4\sqrt{2E_{10}}} a(\mu_-) + O(\lambda^4), \tag{A.13}$$

and the contribution from equation (A.6) is

$$\text{equation (A.6)} \sim \frac{\lambda^2}{8\sqrt{2E_{10}}} a(t_0) + O(\lambda^4 \log \lambda^2). \tag{A.14}$$

As a result, we have the expression

$$\int_{t_1}^{t_0} \mathrm{d}s \frac{a(s)}{\cosh^2 Q} \sim \left(1 - \frac{\lambda^2}{2}\right) \int_{\mu_-}^{t_0} \mathrm{d}s\, a(s). \tag{A.15}$$

In the same way the integral from t_0 to t_2 is evaluated:

$$\int_{t_0}^{t_2} \mathrm{d}s \frac{a(s)}{\cosh^2 Q} \sim \left(1 - \frac{\lambda^2}{2}\right) \int_{t_0}^{\mu_+} \mathrm{d}s\, a(s). \tag{A.16}$$

Combining the results, we get the expression of the integral of V in equation (75).

Next, we integrate the energy gain equation (32) and obtain the approximate expression for the time-dependent energy. We take the energy $E_\alpha(t)$ in equation (A.1) at $t = t_0$ as the reference energy so that the energy gain equation is rewritten as

$$E(t) - E_\alpha(t_0) = \int_{t_0}^{t} \mathrm{d}s \frac{\dot{a}(s)}{\cosh^2 Q(s)}. \tag{A.17}$$

For convenience for applying the adiabatic approximation in the regions, $(\mathrm{Re}\, \mu_- < \mathrm{Re}\, t < \mathrm{Re}\, t_0)$ and $(\mathrm{Re}\, t_0 < \mathrm{Re}\, t < \mathrm{Re}\, \mu_+)$, the integral is further reduced as

$$E(t) - E_\alpha(t) = \int_{t_0}^{t} \mathrm{d}s \left\{ \frac{\dot{a}(s)}{\cosh^2 Q(s)} - \dot{E}_\alpha(s) \right\}, \tag{A.18}$$

where $\dot{E}_\alpha(t) \sim \dot{a}(t)(1 - \alpha^2/2\sqrt{a(t)})$. As before, we substitute the unperturbed solution equation (23) into equation (A.18) and make an approximation including terms of up to α^2, which result in

$$\begin{aligned} E(t) - E_\alpha(t) &\sim \int_{t_0}^{t} \mathrm{d}s \left\{ \frac{\dot{a}(s)}{1 + \lambda^2 \cosh^2(\sqrt{2E_{10}}(s - t_0))} - \dot{E}_\alpha(s) \right\} \\ &\sim \int_0^{t-t_0} \mathrm{d}\tau \left\{ \frac{\dot{a}(t_0 + \tau)}{1 + \frac{\lambda^2}{4} \mathrm{e}^{-2\sqrt{2E_{10}}\tau}} - \dot{a}(t_0 + \tau) \right\} \qquad \text{(A.19)} \\ &\quad - \int_0^{t-t_0} \mathrm{d}\tau s \left\{ \frac{\lambda^2 \dot{a}(t_0 + \tau)}{2\left(1 + \frac{\lambda^2}{4} \mathrm{e}^{-2\sqrt{2E_{10}}\tau}\right)^2} - \frac{\alpha^2 \dot{a}(t_0 + \tau)}{2\sqrt{2a(t_0 + \tau)}} \right\} \qquad \text{(A.20)} \end{aligned}$$

$$-\int_0^{t-t_0} \mathrm{d}\tau \left\{ \frac{\lambda^2 \dot{a}(t_0+\tau)\,\mathrm{e}^{2\sqrt{2E_{10}}\tau}}{4\left(1+\frac{\lambda^2}{4}\,\mathrm{e}^{-2\sqrt{2E_{10}}\tau}\right)^2} \right\}. \tag{A.21}$$

Evaluation of each term of RHS of the above equation is achieved after the recipe described in the integral of V. After a long manipulation, the results in the range $\mathrm{Re}\,t_0 > \mathrm{Re}\,t > \mathrm{Re}\,\mu_-$ are as follows,

$$\text{equation (A.19)} \sim -\frac{\lambda^2}{8}\frac{\dot{a}(t_0)}{\sqrt{2E_{10}}} + \frac{\dot{a}(t)}{2\sqrt{2E_{10}}} \log\left(1+\left(1+\frac{\lambda^2}{2}\right)\mathrm{e}^{-2\sqrt{2E_{10}}(t-\mu_-)}\right), \tag{A.22}$$

$$\text{equation (A.20)} \sim -\frac{\lambda^2}{2} \times \text{equation (A.22)} - \frac{\lambda^2}{8\sqrt{2E_{10}}}\dot{a}(t)(1-\tanh(\sqrt{2E_{10}}(t-\mu_-))), \tag{A.23}$$

$$\text{equation (A.21)} \sim \frac{\lambda^2}{8}\frac{\dot{a}(t_0)}{\sqrt{2E_{10}}} - \frac{\lambda^4}{32}\frac{\dot{a}(t)}{\sqrt{2E_{10}}}\,\mathrm{e}^{2\sqrt{2E_{10}}(t-\mu_-)}. \tag{A.24}$$

The results in the range $\mathrm{Re}\,t < \mathrm{Re}\,\mu_-$ are, on the other hand, given by

$$\begin{aligned}\text{equation (A.19)} \sim\ & a(\mu_-) - a(t) - \frac{\lambda^2}{8}\frac{\dot{a}(t_0)}{\sqrt{2E_{10}}} + \frac{\lambda^2}{4}\frac{\dot{a}(\mu_-)}{\sqrt{2E_{10}}} \\ & + \frac{\dot{a}(t)}{2\sqrt{2E_{10}}} \log\left(1+\left(1-\frac{\lambda^2}{2}\right)\mathrm{e}^{2\sqrt{2E_{10}}(t-\mu_-)}\right),\end{aligned} \tag{A.25}$$

$$\begin{aligned}\text{equation (A.20)} \sim\ & a(t)\frac{\alpha^2}{\sqrt{2a(t)}} - a(\mu_-)\frac{\alpha^2}{\sqrt{2a(\mu_-)}} - \frac{\lambda^2}{4}\frac{\dot{a}(\mu_-)}{\sqrt{2E_{10}}} \\ & - \frac{\lambda^2}{4}\frac{\dot{a}(t)}{\sqrt{2E_{10}}}\left\{\log\left(1+\left(1-\frac{\lambda^2}{2}\right)\mathrm{e}^{2\sqrt{2E_{10}}(t-\mu_-)}\right)\right. \\ & \left. - \left(1+\left(1+\frac{\lambda^2}{2}\right)\mathrm{e}^{-2\sqrt{2E_{10}}(t-\mu_-)}\right)^{-1}\right\},\end{aligned} \tag{A.26}$$

$$\text{equation (A.21)} \sim \frac{\lambda^2}{8}\frac{\dot{a}(t_0)}{\sqrt{2E_{10}}} - \frac{\lambda^4}{32}\frac{\dot{a}(t)}{\sqrt{2E_{10}}}\,\mathrm{e}^{2\sqrt{2E_{10}}(t-\mu_-)}. \tag{A.27}$$

Thanks to the symmetry of the system, evaluation of each term for the ranges $\mathrm{Re}\,\mu_+ > \mathrm{Re}\,t > \mathrm{Re}\,t_0$ and $\mathrm{Re}\,t > \mathrm{Re}\,\mu_+$ is achieved in the same way.

Combining all the results obtained above and ignoring terms of $O(\alpha^2\epsilon\omega)$, we get the resultant expression of $E(t)$ as a function of t in equation (76), and in the limits $t = t_1 \to -\infty$ and $t = t_2 \to +\infty$, equations (77) and (78) are obtained, respectively.

Appendix B. Evaluation of higher order terms in S_S

We evaluate how $\mathrm{Im}\,S_S$ varies as one goes off from the critical point along the set $\mathcal{M}_{\mathcal{R}}$. To this end, we first derive an improved expression for the difference between μ_- and μ_{-c}, which is more accurate than equation (41). Indeed, from equations (43) and (77), we obtain the following expression:

$$\delta\mu_- = \mu_- - \mu_{-c} \sim \frac{a(\mu_{-c})}{\dot{a}(\mu_{-c})}\frac{\alpha^2}{\sqrt{2a(\mu_{-c})}} \sim \frac{\alpha^2 E_1}{\sqrt{2E_1}}\frac{1}{\omega\epsilon\cos(\omega\mu_{-c})} \sim O\left(\frac{\alpha^2}{\omega\epsilon}\right). \tag{B.1}$$

The final order estimation for $\delta\mu_-$ was used throughout the main text. By taking into account the expression for the critical gate $\mu_{-c} \sim (n+3/4)2\pi/\omega + \mathrm{i}\cosh^{-1}\{(1-E_1)/\epsilon(1-\chi(\omega))\}/\omega$, which is obtained by the Melnikov method (χ is defined by equation (26)) [18], equation (B.1) is further reduced to

$$\delta\mu_- \sim \frac{\alpha^2 E_1}{\sqrt{2E_1}} \frac{1}{\mathrm{i}\omega\epsilon \sinh(\omega \mathrm{Im}\,\mu_{-c})}. \tag{B.2}$$

Unless $\mathrm{Im}\,\mu_{-c}$ is extremely large, the estimation as $\cos(\omega\mu_{-c}) \sim O(\omega)$ and $\delta\mu_- \sim O\left(\frac{\alpha^2}{\omega^2\epsilon}\right)$ is available. Indeed, in our numerical calculation, $\mathrm{Im}\,\mu_{-c} \sim \mathrm{Im}\,t_1 \sim 2.57$, then it might be the case and better to adopt the estimation $\delta\mu_- \sim O\left(\frac{\alpha^2}{\omega^2\epsilon}\right)$.

The trajectory starting from $\mathcal{M}_\mathcal{R}$ at t_1, which is deviated from t_{1c} by a very small amount α^2/A_1 (see eq(41)), arrives at the final manifold with a given energy E_2. Such a trajectory goes through the exit gate μ_+, and arrives at the final manifold, closely following the unstable manifold W_u. On the other hand, according to the argument in subsection 4.2, there exists a trajectory along W_u which intersects the same final manifold. This trajectory passes through the critical exit gate μ_{+c}, and hence μ_{+c} and μ_+ are closely connected in the same way as μ_{-c} and μ_- thanks to the symmetry of time evolution around t_0. Let us consider the branch $\mathcal{M}_\mathcal{R}$, whose $\mathcal{L}_\mathcal{S}$-set very closely follows the real unstable manifold. Since $\mu_{+c} \in \mathbf{R}$, from $E_2 = a(\mu_{+c})$ and equation (78), the deviation $\delta\mu_+ = \mu_+ - \mu_{+c}$ is estimated as

$$\delta\mu_+ \sim \begin{cases} \dfrac{a(\mu_{+c})}{\dot{a}(\mu_{+c})}\dfrac{\alpha^2}{\sqrt{2a(\mu_{+c})}} \sim \dfrac{\alpha^2 E_2}{\sqrt{2E_2}}\dfrac{1}{\omega\epsilon\cos(\omega\mu_{+c})} & \\ \sim O\left(\dfrac{\alpha^2}{\epsilon\omega}\right) & (\text{if} \quad \dot{a}(\mu_{+c}) \neq 0 \text{ and } \mu_{+c} \in \mathbf{R}) \\ \dfrac{2a(\mu_{+c})}{\ddot{a}(\mu_{+c})}\dfrac{\alpha^2}{\sqrt{2a(\mu_{+c})}} \sim O\left(\dfrac{\alpha^2}{\omega^2\epsilon}\right) & (\text{if} \quad \dot{a}(\mu_{+c}) = 0 \text{ and } \mu_{+c} \in \mathbf{R}). \end{cases} \tag{B.3}$$

Making a more precise expression than equation (40), which provides the relation between μ_- and t_1 together with that between μ_{-c} and t_{1c}, and subtracting one from the other yield

$$\delta t_1 \equiv t_1 - t_{1c} \sim (1 + O(\epsilon\omega^2))\delta\mu_- + \frac{\alpha^2}{8E_1} \sim \delta\mu_-, \tag{B.4}$$

and the symmetry of time evolution guarantees the relation

$$\delta t_2 \equiv t_2 - t_{2c} \sim (1 + O(\epsilon\omega^2))\delta\mu_+ - \frac{\alpha^2}{8E_2} \sim \delta\mu_+, \tag{B.5}$$

where t_{2c} is the time at which the trajectory of μ_{+c} arrives at Q_2.

Now we evaluate the deviation of $\mathrm{Im}\,S_S$ when t_1 is moved along $\mathcal{M}_\mathcal{R}$ from the critical point t_{1c}. From equation (80), the deviation is given by

$$\begin{aligned} &\mathrm{Im}\,\Delta S_S = \mathrm{Im}\,S_S(t_1) - \mathrm{Im}\,S_S(t_{1c}) \sim \sum_{i=1}^{6} I_i, \\ &I_1 = \mathrm{Im}\,\frac{\epsilon}{\omega}((\cos\omega\mu_+ - \cos\omega\mu_-) - (\cos\omega\mu_{+c} - \cos\omega\mu_{-c})), \\ &I_2 = +2E_1\mathrm{Im}((\mu_- - t_1) - (\mu_{-c} - t_{1c})) + 2E_2\mathrm{Im}((t_2 - \mu_+) - (t_{2c} - \mu_{+c})), \\ &I_3 = -\mathrm{Im}(\mu_- - \mu_{-c})(E_1 - 1) + \mathrm{Im}(\mu_+ - \mu_{+c})(E_2 - 1), \\ &I_4 = +\mathrm{Im}\int_{\mu_-}^{\mu_+}\left(\frac{\alpha^2}{\sqrt{2E_{10}}} - \frac{\alpha^2}{\sqrt{2a(t)}}\right)a(t)\,\mathrm{d}t, \\ &I_5 = +\mathrm{Im}\left(\frac{\dot{a}(\mu_-)}{4E_{10}} - \frac{\dot{a}(\mu_{-c})}{4}\right)\frac{\pi^2}{12} - \mathrm{Im}\frac{\dot{a}(\mu_+)}{4E_{10}}\frac{\pi^2}{12}. \end{aligned} \tag{B.6}$$

The order of magnitude of each term on the RHS of the above equation is estimated as follows:

$$\begin{aligned}
I_1 &\sim -\mathrm{Im}\,\epsilon(\delta\mu_+ \sin\omega\mu_{+c} - \delta\mu_- \sin\omega\mu_{-c}) \\
&\sim \mathrm{Im}(1-E_2)\delta\mu_+ - \mathrm{Im}(1-E_1)\delta\mu_- \sim O(\epsilon)\times O(\delta t_1), \\
I_2 &\sim \mathrm{Im}(O(\epsilon\omega^2)\delta\mu_- - \alpha^2/4 - O(\epsilon\omega^2)\delta\mu_+ - \alpha^2/4) \\
&\sim O(\epsilon\omega^2)\times O(\delta t_1), \\
I_3 &\sim \mathrm{Im}(1-E_1)\delta\mu_- - \mathrm{Im}(1-E_2)\delta\mu_+ \\
&\sim O(\epsilon)\times O(\delta t_1), \\
I_4 &\sim \mathrm{Im}\int_{\mu_-}^{\mu_+}(O(\alpha^4)+O(\epsilon\alpha^2))a(t)\,\mathrm{d}t \\
&\sim \mathrm{Im}((\mu_+-\mu_-)(O(\alpha^4)+O(\epsilon\alpha^2)) \sim (O(\alpha^4\log\alpha)+O(\epsilon\alpha^2\log\alpha)), \\
I_5 &\sim O(\epsilon\omega^2)\times O(\delta t_1).
\end{aligned}$$

I_1 and I_3 are in the same order of $O(\epsilon)\times O(\delta t_1)$ and dominate others, but they cancel out in $O(\epsilon)\times O(\delta t_1)$. An improved calculation taking higher order corrections into account, for example, by making use of $E_{1,2} = a(\mu_{\mp c}) - \epsilon\chi(\omega)\sin\omega\mu_{\mp c} \sim a(\mu_{\mp c}) + O(\epsilon\omega^2)$, results in

$$I_1 + I_3 \sim O(\epsilon\omega^2)\times O(\delta t_1) + O(\epsilon\omega^2)\times O(\delta t_1^2). \tag{B.7}$$

Note that the second most dominant terms I_2 and I_5 are of $O(\epsilon\omega^2)\times O(\delta t_1)$. Therefore, the estimation

$$\mathrm{Im}\,\Delta S_S \sim O(\epsilon\omega^2)\times|\delta t_1| + O(\epsilon\omega^2)\times|\delta t_1|^2 \tag{B.8}$$

is obtained. When $\delta t_1 \sim \delta\mu_\pm \sim O(\alpha^2/\epsilon\omega)$, the result may be rewritten as

$$\mathrm{Im}\,\Delta S_S \sim O(\epsilon\omega^2)\times|\delta t_1| + O(\epsilon\omega)\times|\delta t_1|^2. \tag{B.9}$$

Appendix C. Evaluation of amplitude factor

Equation (78) indicates that E_2 is a function of μ_+. Furthermore, μ_+ is a function of t_1 (or δt_1) from equations (44) and (B.1). Thus the partial derivative $\partial E_2/\partial t_1$ immediately leads to

$$\frac{\partial E_2(Q_2, Q_1, E_1, t_1)}{\partial t_1} = \frac{\partial\mu_+}{\partial t_1}\dot{a}(\mu_+)\left(1 - \frac{1}{2}\frac{\alpha^2}{\sqrt{2a(\mu_+)}}\right) - \frac{A_1}{2}\sqrt{2a(\mu_+)}. \tag{C.1}$$

Next we see how μ_+ depends explicitly on t_1. Equation (44) is rewritten as

$$\mu_+ \sim \mu_- - \tfrac{1}{\sqrt{2}}\log(A_1(t_1 - t_{1c})) + C + \Delta\mu, \tag{C.2}$$

by using equation (41), where C is a constant and $\Delta\mu$ is a periodic function of the period T, whose derivative gives only a small contribution of $O(\epsilon)$. Since the particle moves freely for $\mathrm{Re}\,t < \mathrm{Re}\,\mu_-$ with the constant momentum P_1, μ_- is well approximated by $\sim t_1 + \mathrm{const.}$ (see equation (40)). We thus obtain

$$\frac{\partial\mu_+}{\partial t_1} \sim 1 - \frac{A_1}{\sqrt{2}\alpha^2} + O(\epsilon) \sim 1 - \frac{1}{\sqrt{2}(t_1 - t_{1c})}. \tag{C.3}$$

Putting it into equation (C.1) yields

$$\frac{\partial E_2(Q_2, Q_1, E_1, t_1)}{\partial t_1} \sim \left(1 - \frac{1}{\sqrt{2}(t_1 - t_{1c})}\right)\dot{a}(\mu_+)\left(1 - \frac{1}{2}\frac{\alpha^2}{\sqrt{2a(\mu_+)}}\right) - \frac{A_1}{2}\sqrt{2a(\mu_+)}. \tag{C.4}$$

Substituting it into equation (16) and ignoring $O(\alpha^2\epsilon\omega)$, we get equation (84).

References

[1] Bohigas O, Tomsovic S and Ullmo D 1990 *Phys. Rev. Lett.* **65** 5
Bohigas O, Tomsovic S and Ullmo D 1993 *Phys. Rep.* **223** 45

[2] Brodier O, Schlagheck P and Ullmo D 2001 *Phys. Rev. Lett.* **87** 064101
Brodier O, Schlagheck P and Ullmo D 2002 *Ann. Phys., NY* **300** 88
Eltschka C and Schlagheck P 2005 *Phys. Rev. Lett.* **94** 014101

[3] Creagh S C 1998 Tunneling in two dimensions *Tunneling in Complex Systems* ed S Tomsovic (Singapore: World Sientific) pp 35–100

[4] Ankerhold J 2007 *Quantum Tunneling in Complex Systems The Semiclassical Approach* (Berlin: Springer)

[5] Hensinger W K *et al* 2001 Dynamical tunneling of ultracold atoms *Nature* **412** 52–5

[6] Steck D A, Oskay W H and Raizen M G 2001 Observation of chaos-assisted tunneling between islands of stability *Science* **293** 274–8

[7] Dembowski C *et al* 2000 First experimental evidence for chaos-assisted tunneling in a microwave annular Billiard *Phys. Rev. Lett.* **84** 867

[8] Miller W H 1970 *J. Chem. Phys.* **53** 1949
Miller W H 1974 *Adv. Chem. Phys.* **25** 69

[9] Miller W H and George T F 1972 *J. Chem. Phys.* **56** 5668
George T F and Miller W H 1972 *J. Chem. Phys.* **57** 2458

[10] Wilkinson M 1986 *Physica* D **21** 341
Wilkinson M and Hannay J H 1987 *Physica* D **27** 201

[11] Creagh S C and Whelan N D 1996 *Phys. Rev. Lett.* **77** 4975
Creagh S C and Whelan N D 1999 *Phys. Rev. Lett.* **82** 5237
Creagh S C and Whelan N D 2000 *Phys. Rev. Lett.* **84** 4084

[12] Creagh S C 2004 *Nonlinearity* **17** 1261
Creagh S C 2005 *Nonlinearity* **18** 2089
Drew C S, Creagh S C and Tew R H 2005 *Phys. Rev.* A **72** 062501

[13] Adachi S 1989 *Ann. Phys., NY* **195** 45

[14] Shudo A and Ikeda K S 1995 *Phys. Rev. Lett.* **74** 682
Shudo A and Ikeda K S 1998 *Physica* D **115** 234
Onishi T, Shudo A, Ikeda K S and Takahashi K 2001 *Phys. Rev.* E **64** 025201
Onishi T, Shudo A, Ikeda K S and Takahashi K 2003 *Phys. Rev.* E **68** 056211

[15] Shudo A and Ikeda K S 1996 *Phys. Rev. Lett.* **76** 4151

[16] Shudo A, Ishii Y and Ikeda K S 2002 *J. Phys. A: Math. Gen.* **35** L225 and forthcoming papers

[17] Takahashi K and Ikeda K S 2000 *Ann. Phys., NY* **283** 94

[18] Takahashi K and Ikeda K S 2003 *J. Phys. A: Math. Gen.* **36** 7953

[19] Takahashi K and Ikeda K S 2005 *Europhys. Lett.* **71** 193
Takahashi K and Ikeda K S 2006 *Europhys. Lett.* **75** 355 (erratum)

[20] Takahashi K and Ikeda K S 2006 *Phys. Rev. Lett.* **97** 240403 and forthcoming papers

[21] Schulman L S 1981 *Techinques and Applications of Path Integration* (New York: Wiley)

[22] Takahashi K, Yoshimoto A and Ikeda K S 2002 *Phys. Lett.* A **297** 370

[23] Yoshimoto A 2000 *Rep. Math. Phys.* **46** 303

[24] Takahashi K and Ikeda K S 1997 *J. Chem. Phys.* **106** 4463

[25] Takahashi K and Ikeda K S 2001 *Found. Phys.* **31** 177

[26] Stokes G G 1864 *Trans. Cmbridge Philos. Soc.* **10** 106
Dingle R B 1973 *Asymptotic Expansions: Their Derivation and Interpretation* (London: Academic)
For a very recent development on the study of Stokes phenomenon, see, for example Sternin B Y and Shatalov V E 1996 *Borel-Laplace Transform and Asymptotic Theory* (Boca Raton, FL: CRC Press)

[27] Takahashi K and Ikeda K S, in preparation

[28] Davis M J and Gray S K 1986 Bottlenecks to unimolecular reactions and an alternative form for classical RRKM theory *J. Chem. Phys.* **84** 5389–411

[29] Wiggins S, Wiesenfeld L, Jaffé C and Uzer T 2001 *Phys. Rev. Lett.* **86** 5478
Uzer T, Jaffe C, Palacian J, Yanguas P and Wiggins S 2002 *Nonlinearity* **15** 957–92

[30] Toda M, Komatsuzaki T, Konishi T and Berry R S (ed) 2005 *Geometric Structures on Phase Space in Multi-Dimensional Chaos, Application to Chemical Reaction Dynamics in Complex Systems (Adv. Chem. Phys.* vol 130*)*

[31] Jaffé C, Farrelly D and Uzer T 1999 *Phys. Rev.* A **60** 3833
Jaffé C, Farrelly D and Uzer T 2000 *Phys. Rev. Lett.* **84** 610

[32] Bedford E and Smillie J 1991 *J. Am. Math. Soc.* **4** 657